1 # Cloud Drop Number Concentrations over the Western North Atlantic
2 # Ocean: Seasonal Cycle, Aerosol Interrelationships, and Other
3 # Influential Factors

5 Hossein Dadashazar[1], David Painemal[2,3], Majid Alipanah[4], Michael Brunke[5], Seethala Chellappan[6], Andrea
6 F. Corral[1], Ewan Crosbie[2,3], Simon Kirschler[7], Hongyu Liu[8], Richard Moore[2], Claire Robinson[2,3], Amy Jo
7 Scarino[2,3], Michael Shook[2], Kenneth Sinclair[9,10], K. Lee Thornhill[2], Christiane Voigt[7], Hailong Wang[11],
8 Edward Winstead[2,3], Xubin Zeng[5], Luke Ziemba[2], Paquita Zuidema[6], Armin Sorooshian[1,5]

10 [1]Department of Chemical and Environmental Engineering, University of Arizona, Tucson, AZ, USA
11 [2]NASA Langley Research Center, Hampton, VA, USA
12 [3]Science Systems and Applications, Inc., Hampton, VA, USA
13 [4]Department of Systems and Industrial Engineering, University of Arizona, Tucson, AZ, USA
14 [5]Department of Hydrology and Atmospheric Sciences, University of Arizona, Tucson, AZ, USA
15 [6]Rosenstiel School of Marine and Atmospheric Science, University of Miami, Miami, FL, USA
16 [7]Institute of Atmospheric Physics, German Aerospace Center
17 [8]National Institute of Aerospace, Hampton, VA, USA
18 [9]NASA Goddard Institute for Space Studies, New York, NY, USA
19 [10]Universities Space Research Association, Columbia, MD, USA
20 [11]Atmospheric Sciences and Global Change Division, Pacific Northwest National Laboratory, Richland,
21 WA, USA

23 *Correspondence to: Hossein Dadashazar (hosseind@arizona.edu)
24

26 **Abstract**. Cloud drop number concentrations (N_d) over the western North Atlantic Ocean (WNAO) are
27 generally highest during the winter (DJF) and lowest in summer (JJA), in contrast to aerosol proxy variables
28 (aerosol optical depth, aerosol index, surface aerosol mass concentrations, surface cloud condensation nuclei
29 [CCN] concentrations) that generally peak in spring (MAM) and JJA with minima in DJF. Using aircraft,
30 satellite remote sensing, ground-based in situ measurements data as well as reanalysis data, we characterize
31 factors explaining the divergent seasonal cycles and furthermore probe into factors influencing N_d on
32 seasonal time scales. The results can be summarized well by features most pronounced in DJF, including
33 features associated with cold air outbreak (CAO) conditions such as enhanced values of CAO index,
34 planetary boundary layer height (PBLH), low-level liquid cloud fraction, and cloud-top height, in addition to
35 winds aligned with continental outflow. Data sorted into high and low N_d days in each season, especially in
36 DJF, revealed that all of these conditions were enhanced on the high N_d days, including reduced sea level
37 pressure and stronger wind speeds. Although aerosols may be more abundant in MAM and JJA, the
38 conditions needed to activate those particles into cloud droplets are weaker than in colder months, which is
39 demonstrated by calculations of strongest (weakest) aerosol indirect effects in DJF (JJA) based on comparing
40 N_d to perturbations in four different aerosol proxy variables (total and sulfate aerosol optical depth, aerosol
41 index, surface mass concentration of sulfate). We used three machine learning models and up to 12 input
42 variables to infer about most influential factors related to N_d for DJF and JJA, with the best performance
43 obtained with gradient boosted regression tree (GBRT) analysis. The model results indicated that cloud
44 fraction was the most important input variable, followed by some combination (depending on season) of
45 CAO index and surface mass concentrations of sulfate and organic carbon. Future work is recommended to
46 further understand aspects uncovered here such as impacts of free tropospheric aerosol entrainment on clouds,
47 wet scavenging and giant CCN effects on aerosol-N_d relationships, updraft velocity, and vertical structure of
48 cloud properties such as adiabaticity that impact the satellite estimation of N_d.
49
50
51

1. Introduction

Aerosol indirect effects remain the dominant source of uncertainty in estimates of total anthropogenic radiative forcing (Myhre et al., 2013; Boucher et al., 2013). Central to these effects is knowledge about cloud drop number concentration (N_d), as it is the connection between the subset of particles that activate into drops (cloud condensation nuclei, CCN) and cloud properties. It is widely accepted that warm clouds influenced by higher number concentrations of aerosol particles have elevated N_d and smaller drops (all else held fixed), potentially resulting in enhanced cloud albedo (Twomey, 1977), suppressed precipitation (Albrecht, 1989), and increased vulnerability to overlying air resulting from enhanced cloud top entrainment (Ackerman et al., 2004).

Reducing uncertainty in how aerosols and clouds interact within a given meteorological context requires accurate estimates of N_d and aerosol concentrations and properties. Since intensive field studies struggle to obtain broad spatial and temporal coverage of such data, satellite remote sensing and reanalysis datasets are relied on for studies examining intra- and interannual features over large spatial areas. Limitations of satellite retrievals are important to recognize. N_d is not directly retrieved but derived using other parameters (e.g., cloud optical depth, cloud drop effective radius, cloud top temperature) and with assumptions about cloud adiabatic growth and N_d being vertically constant (Grosvenor et al., 2018). Aerosol number concentrations are usually represented by a columnar parameter such as aerosol optical depth (AOD) and thus not directly below clouds, which is the aerosol layer most likely to interact with the clouds. Furthermore, aerosol data are difficult to retrieve in cloudy columns. Reanalysis datasets circumvent issues for the aerosol parameters as they provide vertically-resolved data (e.g., surface layer and thus below clouds) and are available for cloudy columns.

Of special interest in this work is the western North Atlantic Ocean (WNAO) where decades of extensive research have been conducted for topics largely unrelated to aerosol-cloud interactions (Sorooshian et al., 2020), thereby providing opportunity for closing knowledge gaps for this area in a region with a wide range of aerosol and meteorological conditions (Corral et al., 2021; Painemal et al., 2021). Past work showed different seasonal cycles of AOD and N_d in this region (Sorooshian et al., 2019; Grosvenor et al., 2018), which partly motivates this study to unravel why N_d behaves differently on seasonal time scales. A previous study investigating seasonal cycles of N_d in the North Atlantic region found that cloud microphysical properties were primarily dependent on CCN concentrations while cloud macrophysical properties were more dependent on meteorological conditions (e.g., Sinclair et al., 2020). However, due to the complexity of interactions involved and the co-variability between individual components, the magnitude and sign of these feedbacks remain uncertain.

This study uses a multitude of datasets to characterize the N_d seasonal cycle and factors related to N_d variability. The structure of the results and discussion are as follows: (i) case study flight highlighting the wide range of N_d in wintertime and factors potentially affecting that variability; (ii) seasonal cycle of N_d and aerosol concentrations based on different proxy variables; (iii) seasonal cycles of factors potentially influential for N_d such as aerosol size distribution, vertical distribution of aerosol, humidity effects, and aerosol-cloud interactions; (iv) composite analysis of influential factors on "high" and "low" N_d days in each season; (v) modeling analysis to probe more deeply into N_d relationships with other parameters for winter and summer seasons; and (vi) discussion of other factors relevant to N_d unexplored in this work.

2. Methods

2.1 Study Region

We focus on the WNAO, defined here as being bounded by $25° - 50°N$ and $60° - 85°W$. A subset of the results focuses on 6 individual sub-domains representative of different parts of the WNAO (shown later), with five just off the East Coast extending from south to north (South = S, Central-South = C-S, Central = C, Central-North = C-N, North = N) and one over Bermuda.

2.2 Datasets

2.2.1 Satellite Observations (CERES-MODIS/CALIPSO)

Relevant cloud parameters were obtained from the Clouds and the Earth's Radiant Energy System (CERES) edition 4 products (Minnis et al., 2011; Minnis et al., 2020), which are based on the application of CERES's retrieval algorithms on the radiances measured by the MODerate resolution Imaging Spectroradiometer (MODIS) instrument aboard the Aqua satellite. Level 3 daily cloud properties at $1° \times 1°$ spatial resolution (listed in Table 1) were used for the period between January 2013 and December 2017 from CERES-MODIS edition 4 Single Scanning Footprint (SSF) products (Loeb et al., 2016).

N_d is estimated based on an adiabatic cloud model (Grosvenor et al., 2018):

$$N_d = \frac{\sqrt{5}}{2 \pi k} \left(\frac{f_{ad} \, C_w \, \tau}{Q_{ext} \, \rho_w \, r_e^5}\right)^{1/2} \tag{1}$$

where τ is cloud optical depth and r_e is cloud drop effective radius, both of which are obtained from CERES-MODIS for low-level (i.e., surface to 700 hPa) liquid clouds. Q_{ext} is the unitless extinction efficiency factor, assumed to be 2 for liquid cloud droplets, and ρ_w is the density of water (1 g cm^{-3}). Methods described in Painemal (2018) were used to estimate parameters in Eq. 1 as follows: (i) adiabatic water lapse rate (C_w) was determined using cloud top pressure and temperature provided by CERES-MODIS; (ii) the N_d estimation is often corrected for the sub-adiabatic profile by applying the adiabatic value (f_{ad}), but in this work, a value of $f_{ad} = 1$ was assumed due to both lack of consensus on its value and its relatively minor impact on N_d estimation (Grosvenor et al., 2018); and (iii) k parameter representing the width of the droplet spectrum was assumed to be 0.8 over the ocean. Statistics of N_d are often estimated after screening daily observations based on cloud fractions (Wood, 2012; Grosvenor et al., 2018). The purpose of such filters is to reduce the uncertainties associated with the estimation of N_d (Eq. 1) driven by the errors in the retrieval of r_e and τ from MODIS's observed reflectance in a highly heterogeneous cloud field. However, this may unwantedly mask the effects of cloud regime on aerosol-cloud interactions by only including certain low-level cloud types in the analyses (e.g., closed-cell stratocumulus). Therefore, we use all N_d data regardless of cloud fraction with exceptions being Sections 3.5 and 4.2 where a filter of low-level liquid cloud fraction (i.e., CF$_{low-liq.} \geq 0.1$) was applied.

The Cloud-Aerosol Lidar with Orthogonal Polarization (CALIOP) instrument aboard the Cloud-Aerosol Lidar and Infrared Pathfinder Satellite Observations (CALIPSO) provides data on the vertical distribution of aerosols (Winker et al., 2009). Nighttime extinction profiles were acquired from Level 2 version 4.20 products (i.e., 5 km aerosol profile data), between January 2013 and December 2017. We averaged the Level 2 daily extinctions in different $4° \times 5°$ sub-domains (shown later) to obtain the seasonal profiles after applying the screening scheme outlined in Tackett et al. (2018).

Table 1: Summary of various data products used in this study.

Parameter	Data Source	Spatial resolution	Vertical level	Date Range		Spatial Area	Temporal resolution
Cloud optical thickness	CERES-MODIS	1°×1°	NA	01-Jan-2013	31-Dec-2017	60°-85°W; 25°-50°N	Daily
Cloud effective radius	CERES-MODIS	1°×1°	NA	01-Jan-2013	31-Dec-2017	60°-85°W; 25°-50°N	Daily
Cloud fraction	CERES-MODIS	1°×1°	NA	01-Jan-2013	31-Dec-2017	60°-85°W; 25°-50°N	Daily
Cloud top temperature	CERES-MODIS	1°×1°	NA	01-Jan-2013	31-Dec-2017	60°-85°W; 25°-50°N	Daily
Cloud effective height	CERES-MODIS	1°×1°	NA	01-Jan-2013	31-Dec-2017	60°-85°W; 25°-50°N	Daily
Cloud top pressure	CERES-MODIS	1°×1°	NA	01-Jan-2013	31-Dec-2017	60°-85°W; 25°-50°N	Daily
Precipitation	PERSIANN-CDR	1°×1°	NA	01-Jan-2013	31-Dec-2017	60°-85°W; 25°-50°N	Daily
Aerosol extinction (532 nm)	CALIPSO/CALIOP	5 km	NA	01-Jan-2013	31-Dec-2017	60°-85°W; 25°-50°N	Daily
Total aerosol extinction AOT (550 nm)	MERRA-2	1°×1°	NA	01-Jan-2013	31-Dec-2017	60°-85°W; 25°-50°N	Daily
Total aerosol Angstrom parameter (470-870 nm)	MERRA-2	1°×1°	NA	01-Jan-2013	31-Dec-2017	60°-85°W; 25°-50°N	Daily
Sulfate extinction AOT (550 nm)	MERRA-2	1°×1°	NA	01-Jan-2013	31-Dec-2017	60°-85°W; 25°-50°N	Daily
Sea-salt extinction AOT (550 nm)	MERRA-2	1°×1°	NA	01-Jan-2013	31-Dec-2017	60°-85°W; 25°-50°N	Daily
Dust extinction AOT (550 nm)	MERRA-2	1°×1°	NA	01-Jan-2013	31-Dec-2017	60°-85°W; 25°-50°N	Daily
Organic carbon extinction AOT (550 nm)	MERRA-2	1°×1°	NA	01-Jan-2013	31-Dec-2017	60°-85°W; 25°-50°N	Daily
Black carbon extinction AOT (550 nm)	MERRA-2	1°×1°	NA	01-Jan-2013	31-Dec-2017	60°-85°W; 25°-50°N	Daily
Sulfate surface mass concentration	MERRA-2	1°×1°	NA	01-Jan-2013	31-Dec-2017	60°-85°W; 25°-50°N	Daily
Sea-salt surface mass concentration	MERRA-2	1°×1°	NA	01-Jan-2013	31-Dec-2017	60°-85°W; 25°-50°N	Daily
Dust surface mass concentration	MERRA-2	1°×1°	NA	01-Jan-2013	31-Dec-2017	60°-85°W; 25°-50°N	Daily
Organic carbon surface mass concentration	MERRA-2	1°×1°	NA	01-Jan-2013	31-Dec-2017	60°-85°W; 25°-50°N	Daily
Black carbon surface mass concentration	MERRA-2	1°×1°	NA	01-Jan-2013	31-Dec-2017	60°-85°W; 25°-50°N	Daily
Sea level pressure	MERRA-2	1°×1°	Surface	01-Jan-2013	31-Dec-2017	60°-85°W; 25°-50°N	Daily
Geopotential height	MERRA-2	1°×1°	850 hPa	01-Jan-2013	31-Dec-2017	60°-85°W; 25°-50°N	Daily
Sea surface temperature	MERRA-2	1°×1°	Sea surface	01-Jan-2013	31-Dec-2017	60°-85°W; 25°-50°N	Daily
Air temperature	MERRA-2	1°×1°	Surface, 850, 700 hPa	01-Jan-2013	31-Dec-2017	60°-85°W; 25°-50°N	Daily
Relative humidity	MERRA-2	1°×1°	1000-500 hPa	01-Jan-2013	31-Dec-2017	60°-85°W; 25°-50°N	Daily
Wind speed	MERRA-2	1°×1°	2 meter, 950 hPa	01-Jan-2013	31-Dec-2017	60°-85°W; 25°-50°N	Daily
Planetary boundary layer height	MERRA-2	1°×1°	NA	01-Jan-2013	31-Dec-2017	60°-85°W; 25°-50°N	Daily
Vertical pressure velocity	MERRA-2	1°×1°	800 hPa	01-Jan-2013	31-Dec-2017	60°-85°W; 25°-50°N	Daily
Aerosol/Cloud	Airborne: ACTIVATE	-	NA	22-Feb-2020		72.31°-76.64°W; 34.08°-37.16°N	1 Second
CCN-Cape Cod	Ground based measurement	Point measurement	Surface	16-Jul-2012	04-May-2013	70.30°W; 41.67°N	1 Second

2.2.2 MERRA-2

135
136   Aerosol data were obtained from the Modern-Era Retrospective analysis for Research and
137 Applications-Version 2 (MERRA-2) (Gelaro et al., 2017). MERRA-2 is a multidecadal reanalysis where
138 meteorological and aerosol observations are jointly assimilated into the Goddard Earth Observation System
139 version 5 (GEOS-5) data assimilation system (Randles et al., 2017; Buchard et al., 2017). Aerosols in
140 MERRA-2 are simulated with a radiatively coupled version of the Goddard Chemistry, Aerosol, Radiation,
141 and transport model (GOCART; Chin et al., 2002; Colarco et al., 2010). GOCART treats the sources, sinks,
142 and chemistry of 15 externally mixed aerosol mass mixing ratio tracers, which include sulfate, hydrophobic
143 and hydrophilic black and organic carbon, dust (five size bins), and sea salt (five size bins). MERRA-2
144 includes assimilation of bias-corrected Collection 5 MODIS AOD, bias-corrected AOD from the Advanced
145 Very High Resolution Radiometer (AVHRR) instruments, AOD retrievals from the Multiangle Imaging
146 SpectroRadiometer (MISR) over bright surfaces, and ground-based Aerosol Robotic Network (AERONET)
147 direct measurements of AOD (Gelaro et al., 2017). In this study we used total and speciated (i.e., sea-salt,
148 dust, black carbon, organic carbon, and sulfate) AOD at 550 nm between January 2013 and December 2017
149 at times relevant to Aqua's overpass time (13:30 local time). Aerosol index was calculated as the product of
150 AOD and Ångström parameter. MERRA-2 also provides surface mass concentrations of aerosol species
151 including sea-salt, dust, black carbon, organic carbon, and sulfate, which were used as a measure of aerosol
152 levels in the planetary boundary layer (PBL).
153   MERRA-2 data were also used for environmental variables including both thermodynamic (e.g.,
154 temperature and relative humidity) and dynamic parameters (e.g., sea-level pressure (SLP) and geopotential
155 heights) (Gelaro et al., 2017) listed in Table 1. Bilinear interpolation was applied to transfer all MERRA-2
156 variables (Table 1) from their original $0.5° × 0.625°$ spatial resolution to the equivalent $1° × 1°$ grid in
157 CERES-MODIS Level 3 data.
158
2.2.3 Precipitation Data

159
160   Daily precipitation data were obtained from Precipitation Estimation from Remotely Sensed
161 Information using Artificial Neural Networks–Climate Data Record (PERSIANN-CDR) data product
162 (Ashouri et al., 2015; Nguyen et al., 2018). Bilinear interpolation was applied to convert the PERSIANN-
163 CDR data from its native spatial resolution (i.e., $0.25° × 0.25°$) to equivalent $1° × 1°$ grids in CERES-MODIS
164 Level 3 data.
165
2.2.4 Surface-based CCN Data

166
167   Cloud condensation nuclei (CCN) data were obtained from the U.S. Department of Energy's Two-
168 Column Aerosol Project (TCAP) (Berg et al., 2016) to examine the seasonal variations in CCN number
169 concentration at a representative site by Cape Cod, Massachusetts (41.67°N. 70.30°W) over the U.S. East
170 Coast. TCAP was a campaign conducted between June 2012 and June 2013 to investigate aerosol optical and
171 physicochemical properties and interactions between aerosols and clouds (Liu and Li, 2019; Berg et al.,
172 2016). CCN data were available between July 2012 and May 2013 at multiple supersaturations with some
173 gaps in the data collection (i.e., November-December); for simplicity, we focused on CCN data measured at
174 a single supersaturation of 1% owing to relatively better data coverage as compared to lower supersaturations.
175 We note that this higher supersaturation is not necessarily representative of that relevant to the clouds of
176 interest, but is still insightful for understanding the seasonal cycle of CCN concentration. The qualitative
177 seasonal cycle of CCN concentration at 1% matches those at lower supersaturations (e.g., 0.15% – 0.8%).
178
2.2.5 Airborne In-Situ Data

179
180   We used airborne in-situ data collected during the fifth research flight (RF05) of the Aerosol Cloud
181 meTeorology Interactions oVer the western ATlantic Experiment (ACTIVATE) campaign. One flight is used
182 both for simplicity and because it embodied conditions relevant to the discussion of other results. The mission
183 concept involves joint flights between the NASA Langley UC-12 King Air and HU-25 Falcon such that the
184 former flies around 8 – 10 km and the latter flies in the boundary layer to simultaneously collect data on

aerosol, cloud, gas, and meteorological parameters in the same column (Sorooshian et al., 2019). The Falcon flew in a systematic way to collect data at different vertical regions relative to cloud, including the following of relevance to this study: BCB = below cloud base; ACB = above cloud base, BCT = below cloud top, Min. Alt = minimum altitude the plane flies at (500 ft).

This study makes use of the HU-25 Falcon data from the following instruments: Fast Cloud Droplet Probe (FCDP; D_p ~3 – 50 μm) (SPEC Inc.) aerosol and cloud droplet size distributions for quantification of cloud liquid water content (LWC), N_d, and aerosol number concentrations with D_p exceeding 3 μm in cloud-free air (termed FCDP-aerosol); Two Dimensional Stereo (2DS; D_p ~28.5 – 1464.9 μm) (SPEC Inc.) probe for estimation of rain water content (RWC) by integrating raindrop ($D_p \geq$ 39.9 μm) size distributions; Cloud Condensation Nuclei (CCN; DMT) counter for CCN number concentrations; Laser Aerosol Spectrometer (LAS; TSI Model 3340) and Condensation Particle Counter (CPC; TSI model 3772) for aerosol number concentrations with D_p between 0.1 – 1 μm and above 10 nm, respectively; High-Resolution Time-of-Flight Aerosol Mass Spectrometer (AMS; Aerodyne) for submicrometer non-refractory aerosol composition (DeCarlo et al., 2008), operated in 1 Hz Fast-MS mode and averaged to 25-second time resolution; Turbulent Air-Motion Measurement System (TAMMS) for winds and temperature (Thornhill et al., 2003).

CCN, LAS, CPC, and AMS data were collected downstream of an isokinetic double diffuser inlet (BMI, Inc.), whereas the AMS and LAS also sampled downstream of a counterflow virtual impactor (CVI) inlet (BMI, Inc.) when in cloud (Shingler et al., 2012). However, a filter was applied to remove LAS data when the CVI inlet was used. Measurements from the CCN counter, LAS, CPC, and FCDP-aerosol are only shown in cloud-free and rain-free conditions, distinguished by LWC < 0.05 g m^{-3} and RWC < 0.05 g m^{-3}, respectively, and also excluding data collected 20 seconds before and after evidence of rain or cloud. Estimation of supermicromemter particles from FCDP measurements were performed after conducting the following additional screening steps to minimize cloud droplet artifacts: (i) only samples with RH < 98% were included, (ii) data collected during ACB and BCT legs were excluded. CCN, LAS, CPC, and AMS measurements are reported at standard temperature and pressure (i.e., 273 K and 760 torrs) while FCDP and 2DS measurements correspond to ambient conditions.

2.3 Regression Analyses

Regression modeling was conducted to investigate relationships between environmental variables and N_d. The Gradient Boosted Regression Trees (GBRT) model, classified as a machine learning (ML) model, is used, consisting of several weak learners (i.e., regression trees with a fixed size) that are designed and subsequently trained to improve prediction accuracy by fitting the model's trees on residuals rather than response values (Hastie et al., 2009). Desirable characteristics of the GBRT model include both its capacity to capture non-linear relationships and being less vulnerable to overfitting (Persson et al., 2017; Fuchs et al., 2018; Dadashazar et al., 2020). Two separate GBRT models were trained using daily CERES-MODIS N_d data (1° × 1°) in winter (DJF) and summer (JJA) to reveal potential variables impacting N_d. Winter and summer are chosen as they exhibit the highest and lowest N_d concentrations, respectively, among all seasons over the WNAO.

Many variables were picked as input parameters (Table 2) for the GBRT model, categorized as either being aerosol, dynamic/thermodynamic, or cloud variables. Aerosol parameters included MERRA-2 surface mass concentrations for sulfate, sea-salt, dust, and organic carbon. Black carbon concentration was removed from input parameters because of its high correlation ($R^2 = 0.6$) with organic carbon. The following is the list of thermodynamic/dynamic input parameters derived from MERRA-2: vertical pressure velocity at 800 hPa (ω_{800}), planetary boundary layer height (PBLH), cold-air outbreak (CAO) index, relative humidity (RH) in the PBL and free troposphere represented by RH_{950} and RH_{800}, respectively. CAO index is defined as the difference between skin potential temperature (θ_{skt}) and air potential temperature at 850 hPa (θ_{850}) (Papritz et al., 2015). CERES-MODIS cloud parameters include liquid cloud fraction and cloud top height for low-level clouds. In addition, PERSIANN-CDR daily precipitation (Rain) was included as a relevant cloud parameter.

234   Data were split into two sets: training/validation (70%) and testing (30%). Five-fold cross-validation
235 was implemented to train the GBRT model using the training/validation data. Furthermore, both performance
236 and generalizability of the trained models were tested via the aid of the test set, which was not used in the
237 training process. The GBRT models were performed using the scikit-learn module designed in Python
238 (Pedregosa et al., 2011).
239
240 **Table 2: List of input parameters used as predictor variables in the GBRT and linear models. Variables**
241 **are grouped into three general categories.**
242

	Parameter
Aerosol	Sulfate surface mass concentration ($Sulfate_{sf\text{-}mass}$)
	Sea-salt surface mass concentration ($Sea\text{-}salt_{sf\text{-}mass}$)
	Dust surface mass concentration ($Dust_{sf\text{-}mass}$)
	Organic carbon surface mass concentration ($OC_{sf\text{-}mass}$)
Cloud	Low-level liquid cloud fraction ($CF_{low\text{-}liq.}$)
	Low-level liquid cloud-top effective height ($Cloud\text{-}top_{low\text{-}liq.}$)
	Precipitation rate (Rain)
Dynamic/ Thermodynamic	Cold-air outbreak index (CAO_{index}): θ_{skt}*-θ_{850}
	Relative humidity at 950 hPa (RH_{950})
	Relative humidity at 800 hPa (RH_{800})
	Vertical pressure velocity at 800 hPa (ω_{800})
	Planetary boundary layer height (PBLH)

243
244   *Skin potential temperature
245
246   The regression analyses were not performed solely to construct and provide a highly accurate model
247 useful for prediction, but rather to disclose and examine the possible effects of the relevant input variables
248 on N_d considering all the shortcomings of such analyses. For instance, there is some level of interdependency
249 between input variables. To reduce unwanted consequences of correlated features, the interpretation of the
250 results was done with the aid of accumulated local effect (ALE) plots, which are specifically designed to be
251 unbiased to the correlated input variables (Apley and Zhu, 2020). ALE plots illustrate the influence of input
252 variables on the response parameter in ML models. The ALE value of feature S at x_s (i.e., $f_{s,ALE}(x_s)$) can be
253 calculated as follows:
254
255    $$f_{s,ALE}(x_s) = \int_{z_{0,1}}^{x_s} \int_{x_c} f^s(z_s, x_c) \, P(x_c|z_s) dx_c dz_s - constant \qquad (2)$$
256
257 where $f^s(z_s, x_c)$ is the gradient of model's response with respect to variable S (i.e., local effect) and $P(x_c|z_s)$
258 is the conditional distribution of x_c (input features rather than S). $z_{0,1}$ is chosen arbitrarily below the smallest
259 observation of feature S (Apley and Zhu, 2020). The steps in Eq. 2 can be summarized as follows (Molnar,
260 2019; Apley and Zhu, 2020): (i) the average change in the model's prediction is calculated using the
261 conditional distribution of features; (ii) the average change will then be accumulated by integrating it over
262 feature S; and (iii) a constant will be subtracted to vertically center (i.e., the average of ALE becomes zero)
263 the ALE plot. The aforementioned steps, although seemingly complex, assure the avoidance of undesired
264 extrapolation (especially an issue for correlated variables) occurring in alternative approaches such as partial
265 dependence (PD) plots. The value of $f_{s,ALE}(x_s)$ can be viewed as the difference between the model's

266 response at x_s and the average prediction. We used the source code available in https://github.com/blent-
267 ai/ALEPython for the calculation of ALE plots.
268
269 **3. Results and Discussion**
270 **3.1 Aircraft Case Study of N_d Gradient**
271   ACTIVATE Research Flight 5 (RF05) on 22 February 2020 demonstrates the wide range in N_d
272 offshore in the PBL ($\lesssim$ 1.6 km) over the WNAO (Figure 1). On this day, the ACTIVATE study region was
273 dominated by a surface high pressure system centered over the southeastern U.S., with a significant ridge
274 axis extending from the main high to the east-northeast off the Virginia-North Carolina coast and into the
275 WNAO. Aloft, the flight region was located in northwesterly flow behind a trough offshore. This setup led
276 to subsidence in the region and generally clear skies, except where scattered to broken marine boundary layer
277 clouds formed along and east of the Gulf Stream. Two day NOAA HYSPLIT (Rolph et al., 2017; Stein et
278 al., 2015) back trajectories using the "model vertical velocity" method and "REANALYSIS" meteorology
279 data indicate air in the flight region (between 0-3 km) had wrapped around the surface high from the north
280 and left the New England coast 12-24 hours beforehand (with a descending profile). Along the flight segment
281 shown, winds were approximately 6 m s^{-1}, out of the north/northwest during the initial descent, Min. Alt. 1,
282 and BCB1 legs and primarily from the northeast for the other sections of the flight. Sea surface temperatures
283 were 6 – 9°C near the coast during the descent and Min. Alt. 1 leg, 21 – 25°C over the Gulf Stream during
284 the BCB1, ACB1, and BCB2 legs, and 17 – 20°C for the remainder of the flight segment shown. The majority
285 of the segment was in or below the boundary layer clouds, with cloud base around 900 – 1100 m and cloud
286 top around 1750 m. Note that the initial BCB1 leg was much lower at around 460 m, likely reflecting a
287 shallower marine boundary layer and cloud base near the much colder waters close to the coast. Static air
288 temperature ranged between 0 – 10°C, except for the BCT1 leg where temperatures were around -2.3°C.
289
290

291

292
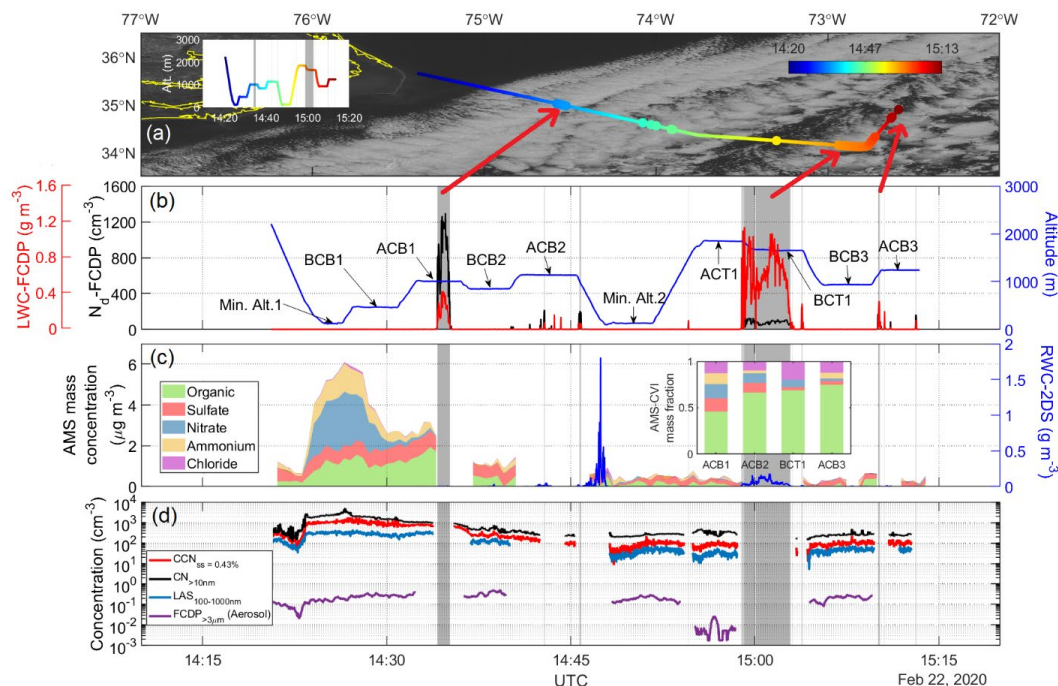
Figure 1: Time series of selected parameters measured by the HU-25 Falcon aircraft during a selected segment of RF05 on 22 February 2020: (a) overlayed flight track on GOES 16 visible imagery obtained at 14:55:04 UTC; (b) altitude, cloud liquid water content (LWC), and N_d, with the latter two obtained from the FCDP; (c) rain water content (RWC) measured by 2DS probe, AMS speciated mass concentration in cloud/rain-free air, and AMS mass fractions for droplet residual particles in cloud as measured downstream of a CVI inlet; (d) number concentrations for CCN at 0.43% supersaturation and particles for three diameter ranges: above 10 nm (CPC), 100-1000 nm (LAS), and above 3 µm (FCDP). Shaded gray areas in (b)-(d) highlight cloudy periods identified as having LWC ≥ 0.05 g m⁻³. Locations of the cloudy regions are pointed to with red arrows in the satellite imagery. Level legs are defined as follows: BCB = below cloud base, ACB = above cloud base, Min. Alt. = minimum altitude the plane flies at (500 ft), ACT = above cloud top, BCT = below cloud top.

N_d values from the FCDP ranged a maximum value of 1298 cm⁻³ closer to the coast during the ACB1 leg (35.00° N, 74.55° W) to a minimum of 19 cm⁻³ farther away in the BCT1 leg (34.32° N, 72.73° W). The minimum N_d value in the ACB3 leg was 85 cm⁻³ (34.11° N, 72.80° W), which is a fairer comparison with the ACB1 leg in terms of being closer to cloud base. The mean N_d values (cm⁻³) in the cloudy portions of the ACB1, BCT1, and ACB3 legs were as follows: 849, 77, 143.

Based on the nearest BCB legs adjacent to the maximum and minimum N_d values (BCB1 = 35.31° N, 74.95° W; BCB3 = 34.41° N, 72.70° W), there was a significant offshore gradient in LAS submicrometer particle number concentration and AMS non-refractory aerosol mass, ranging from 424 cm⁻³ and 5.60 µg m⁻³ (from BCB1) to 21 cm⁻³ and 0.32 µg m⁻³ (from BCB3), respectively; these values are based on times of the maximum and minimum LAS concentrations during the BCB1 and BCB3 legs, respectively. The mean values of submicrometer particle number concentration and AMS non-refractory aerosol for the two BCB legs were as follows: 277 cm⁻³/3.64 µg m⁻³ (BCB1) and 48 cm⁻³/0.42 µg m⁻³ (BCB3). The higher N_d value (1298 cm⁻³) relative to LAS aerosol concentration (424 cm⁻³) at the near-shore point is suggestive of aerosol smaller than 0.1 µm activating into drops. This is supported by the fact that both CCN (supersaturation =

319   0.43%) and CPC number concentrations with $D_p > 10$ nm exhibited mean values of 980 and 1723 cm^{-3} in the
320   BCB1 leg, respectively, dropping to 98 and 260 cm^{-3} in the BCB3 leg. There was a slighter gradient in particle
321   concentrations with $D_p > 3$ μm (most likely sea salt) between the same two points of maximum and minimum
322   LAS concentration in BCB1 and BCB3 legs, respectively: 0.26 cm^{-3} to 0.11 cm^{-3}. For the duration of the
323   flight portion shown in Figure 1, supermicrometer concentrations varied over two orders of magnitude: 0.002
324   – 0.51 cm^{-3}. Sea salt is not expected to follow the same offshore gradient as continentally-derived pollution
325   outflow.
326   Closer to shore during the Min. Alt. 1 leg, nitrate was the dominant aerosol species (~70% mass
327   fraction). Farther offshore during both the BCB1 leg and cloud-free portion of the ACB1 leg, organics were
328   the dominant constituent (~46% mass fraction), whereas farther during the BCB3 leg, the mean mass fraction
329   of sulfate was the highest (75%). Droplet residual particle data show a greater contribution of organics farther
330   offshore, increasing from 46% to 75% between the ACB1 and ACB3 legs, respectively. These composition
331   results, albeit limited to the non-refractory portion of submicrometer aerosol particles, reveal significant
332   changes with distance offshore indicative of varying chemical properties of particles activating into droplets.
333   The cloudy portions of ACB1 are characterized as having little or no rain with maximum RWC value
334   of 0.02 g m^{-3} and mean value of 0.003 g m^{-3}. There is a notable RWC peak at the beginning of the Min. Alt.
335   2 leg, reaching as high as 1.81 g m^{-3} associated with clouds aloft. The precipitation occurrence was also
336   evident in a subsequent BCT1 leg where RWC reached as high as 0.18 g m^{-3}. GOES satellite imagery of the
337   study region (Fig. 1) also reflects the effect of precipitation on cloud morphology where clouds farther
338   offshore resemble open-cell structures. Associated scavenging of particles through the washout process is
339   presumed to contribute to the decline in aerosol concentrations with distance offshore.
340   Figure 1 shows changes in aerosol characteristics coincident with the large gradient in N_d. While
341   ACTIVATE airborne data collection is ongoing to build flight statistics over multiple years, the wide changes
342   in microphysical properties in RF05 motivate looking at other datasets with broader spatiotemporal coverage
343   to learn about potential seasonally-dependent drivers of N_d, including meteorological parameters that vary
344   throughout the year. Furthermore, other datasets can provide insight into the source(s) of seasonal
345   discrepancy between columnar aerosol remote sensing parameters and N_d.

347   **3.2 Seasonal Cycles of N_d and AOD**
348   Figure 2 illustrates the seasonal differences in MERRA-2 AOD and CERES-MODIS N_d over the
349   WNAO that partly motivate this study. Seasonal mean values (± standard deviation) of AOD/N_d (cm^{-3}) were
350   as follows for the entire WNAO: DJF = 0.11 ± 0.03/64.1 ± 18.0; MAM = 0.16 ± 0.03/60.4 ± 13.1; JJA= 0.15
351   ± 0.03/49.1 ± 10.1; SON = 0.11 ± 0.03/50.3 ± 13.9. In contrast to AOD, N_d values and low-cloud fraction
352   (Figure 2c) were highest in DJF and lowest in JJA. DJF showed notably high N_d near the coast, qualitatively
353   consistent with the airborne data. The seasons with the greatest AOD values, accompanied by the most
354   pronounced spatial gradient offshore, were JJA and MAM. The offshore gradient owes to continental
355   pollution outflow (Corral et al., 2021 and references therein). In contrast, DJF and SON exhibited lower AOD
356   values with a distinct area of higher AOD values offshore between ~35° – 40° N accounted for by sea salt.
357   MERRA-2 speciated AOD data (Figure S1) indicate that sea salt and sulfate dominate total AOD regardless
358   of season and that sulfate, organic carbon, and black carbon most closely follow the offshore gradient pattern
359   owing to continental sources. Dust and sea salt have different spatial distributions with the former derived
360   from sources such as North Africa leading to enhanced AODs < 30° N especially in JJA, and sea salt being
361   enhanced offshore especially in JJA.
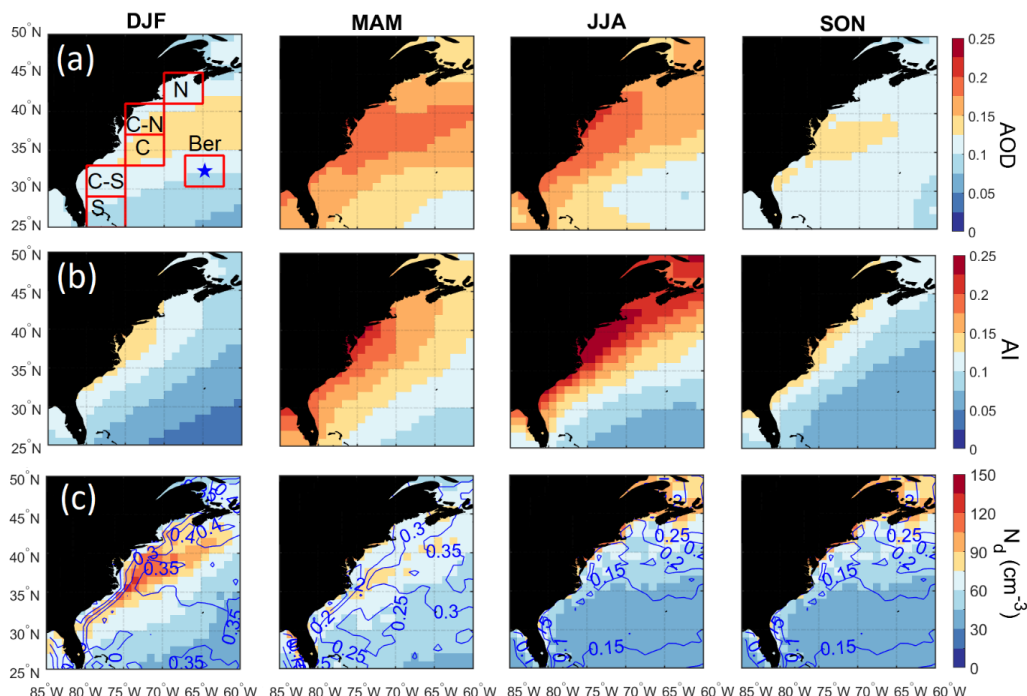
363
364 **Figure 2: Seasonal spatial maps for (a) MERRA-2 aerosol optical depth (AOD), (b) MERRA-2 aerosol**
365 **index (AI), and (c) cloud drop number concentration (N_d) over the western North Atlantic Ocean**
366 **(WNAO). Contours in (c) represent low-level (cloud top pressure > 700 hPa) liquid cloud fraction**
367 **($CF_{low-liq.}$). Cloud data are based on daily Level 3 data from CERES-MODIS. The maps are based on**
368 **data between January 2013 and December 2017. The boxes in top left panel represent sub-domains**
369 **examined in more detail throughout the study, with the blue star denoting Bermuda.**
370
371 Table 3 probes deeper into individual WNAO sub-domains to compare seasonal AOD and N_d values.
372 For the six sub-domains in Figure 2, MERRA-2 AOD peaks in MAM and JJA, while N_d peaks in DJF. The
373 Bermuda sub-domain was unique in that mean N_d was slightly higher in MAM (53 cm^{-3}) as compared to DJF
374 (48 cm^{-3}). We attribute the slightly different seasonal cycle over Bermuda to its remote nature leading to
375 differences in meteorology and aerosol sources between seasons.
376 One factor that could bias AOD towards higher values with disproportionately less impact on N_d is
377 aerosol hygroscopic growth in humid conditions. Table 3 summarizes mean MERRA-2 RH values in the
378 PBL and free troposphere (FT). Results show that while RH is highest in JJA (except for FT of DJF in sub-
379 domain N), differences between seasons were not very large. The maximum difference among the four
380 seasons when considering mean RH in the PBL and FT for all sub-domains ranged between 3% – 9% and
381 7% – 25%, respectively. Consequently, humidity effects on remotely sensed aerosol parameters cannot alone
382 explain the dissimilar seasonal cycle of N_d and AOD, but can plausibly contribute to some extent.
383
384 **3.3 Contrasting AOD and Aerosol Index**
385 While previous studies have pointed to the limitations of AOD as an aerosol proxy (e.g. Gryspeerdt
386 et al., 2017; Painemal et al., 2020), the N_d-AOD anticorrelation at seasonal scale over the WNAO is at odds
387 with findings for other regions supporting the relationship between these two parameters (Quaas et al., 2008;
388 Sekiguchi et al., 2003; Nakajima et al., 2001; Quaas et al., 2006; Penner et al., 2011; Gryspeerdt et al., 2016;
389 Grandey and Stier, 2010) and also that between sulfate and N_d (McCoy et al., 2017; MacDonald et al., 2020;

390 McCoy et al., 2018; Storelvmo et al., 2009; Lowenthal et al., 2004; Boucher and Lohmann, 1995). Values of
391 N_d are influenced by the number concentration of available CCN, which is determined by aerosol properties
392 (size distribution and composition) and supersaturation level. AOD is an imperfect CCN proxy variable
393 because it does not provide information about composition and size distribution, and is sensitive to relative
394 humidity. Aerosol index (AI) is more closely related to CCN as it partially accounts for the size distribution
395 of aerosols (Nakajima et al., 2001; Deuze et al., 2001; Breon et al., 2002; Hasekamp et al., 2019). The
396 sensitivity of AI to size is evident in spatial maps for each season showing more of an offshore gradient (like
397 sulfate AOD in Figure S1) in each season and lacking both the offshore peak in sea salt between ~35° – 40°
398 N and the maximum AOD for dust south of 30°N in JJA. However, when comparing absolute values between
399 the four seasons in Figure 2b, AI exhibits a similar seasonal cycle as AOD, thereby indicating that size
400 distribution alone cannot explain diverging seasonal cycles for N_d and AOD. We next compare N_d to aerosol
401 data in the PBL where CCN more relevant to droplet activation are confined. Size distribution effects in the
402 PBL can instead be more of a factor especially as sea salt is abundant.

403

404 3.4 Aerosol Size Distribution and Vertical Aerosol Distribution
405 Vertical profiles of aerosol extinction coefficient estimated from CALIOP nighttime observations are
406 shown in Figure 3 for the six sub-domains. Shown also are the seasonally representative planetary boundary
407 layer heights (PBLHs) from MERRA-2, with numerical values of both PBLH and fractional AOD
408 contributions to the PBL and FT in Table 3. The CALIOP results indicate that aerosol extinction more closely
409 follows the N_d seasonal cycle with the highest (lowest) values in the PBL during DJF (JJA). However, aerosol
410 extinction coefficient is sensitive to aerosol size distribution and a plausible scenario is that DJF extinction
411 in the PBL is primarily contributed by coarse sea salt particles, which are especially hygroscopic, but do not
412 contribute significantly to number concentration as demonstrated clearly by airborne observations (Figure
413 1). This is supported in part by how DJF is marked by the highest fractional AOD contribution from the PBL
414 (59 – 72%) where sea salt is concentrated. In contrast, JJA has the lowest fractional AOD contribution from
415 the PBL (11.3 – 52.6%). Sub-domains C-N and N exhibit the greatest changes in AOD fraction in the PBL
416 between seasons with a maximum in DJF (59 – 61%) and a minimum in JJA (11 – 19%) suggesting they are
417 relatively more sensitive to the aerosol vertical distribution in leading to contrasting AOD and N_d seasonal
418 cycles. Bermuda stands out as having the highest AOD fractional contributions in the PBL in DJF (72%) and
419 SON (69%) and among the highest seasonal total AODs in those two seasons (0.14 in DJF and 0.10 in SON)
420 assisted in large part from sea salt (Figure S1) (Aldhaif et al., 2021), coincident with high seasonal wind
421 speeds (Corral et al., 2021).

422
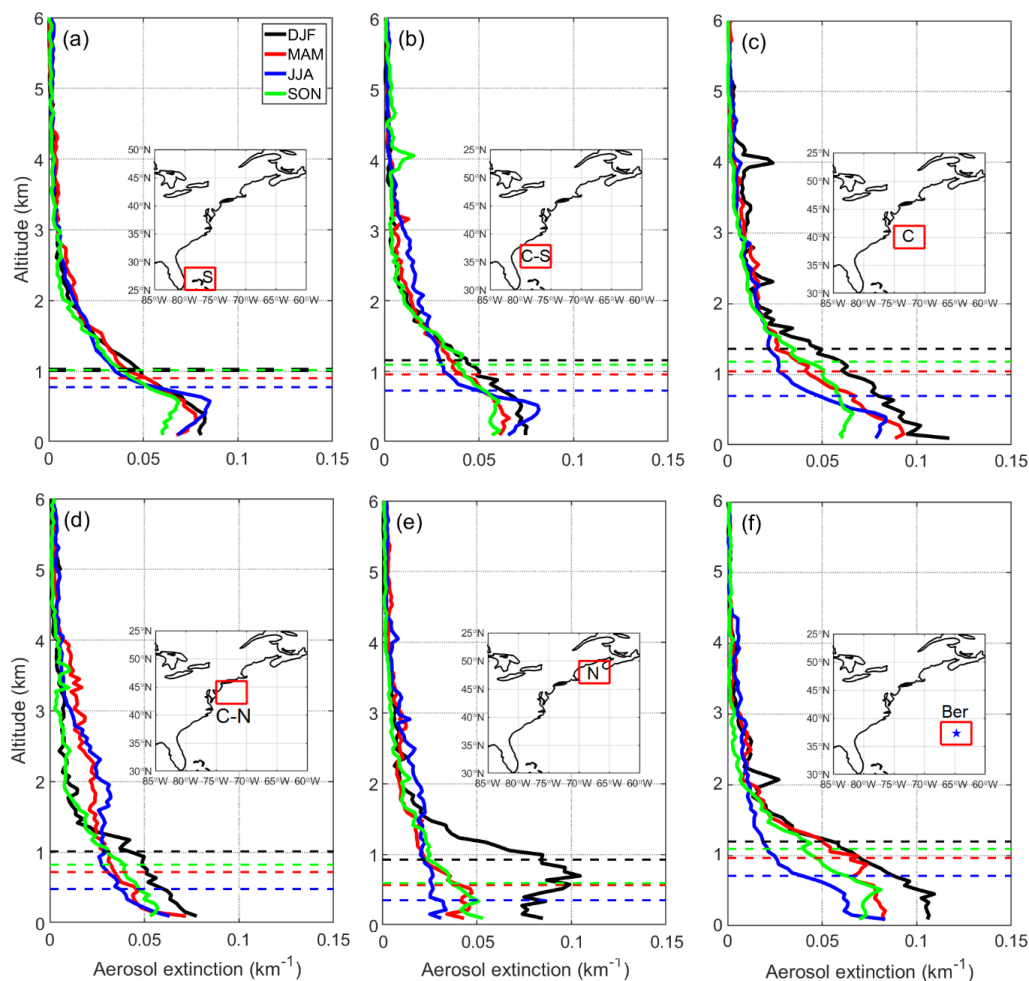
Figure 3: Vertical profiles of CALIPSO aerosol extinction for different seasons in (a-f) six different sub-domains of the WNAO. Average seasonal planetary boundary layer heights (PBLH) from MERRA-2 are denoted with dashed lines.

To explore aerosol number concentration characteristics in the PBL in different seasons, we next discuss results from an opportune dataset over the U.S. East Coast (Cape Cod, MA) providing an annual profile of CCN concentration at 1% supersaturation (Figure 4). Cape Cod is a coastal location representative of the outflow providing an important fraction of the CCN impacting offshore low-level clouds. As the supersaturation examined is relatively high (1%), the measured CCN include smaller particles representing high number concentrations that would not appreciably contribute to the high aerosol extinctions from CALIOP in the PBL in direct contrast to sea salt (i.e., high extinction due to fewer but larger particles). Seasonal mean CCN values do not follow the seasonal cycle of N_d nor CALIOP extinction in the PBL, with values being as follows: DJF = 1436 cm^{-3}; MAM = 1533 cm^{-3}; JJA = 1895 cm^{-3}; SON = 1326 cm^{-3}. These results suggest the following: (i) size distribution effects are significant in the PBL when comparing extinction to number concentration; and (ii) aerosol vertical distribution behavior cannot alone explain the divergent seasonal cycles of N_d and aerosol parameters (e.g., AOD, AI, surface number concentrations).

Table 3: Average drop number concentration (N_d), MERRA-2 AOD, and vertically resolved AOD characteristics from CALIOP for each season over the sub-domains shown in Figure 2. Total CALIOP AOD is shown outside parentheses and numbers inside are the percent AOD fraction in the planetary boundary layer followed by in the free troposphere. Also shown are PBLHs (shown in Figure 3) and the relative humidity in the PBLH and FT.

	S	C-S	C	C-N	N	Bermuda
			$AOD_{MERRA-2}/N_d$ (cm^{-3})			
DJF	0.10/56	0.11/74	0.13/91	0.12/97	0.11/78	0.10/48
MAM	0.14/55	0.17/62	0.18/72	0.19/75	0.16/70	0.14/53
JJA	0.14/41	0.16/43	0.17/47	0.19/68	0.17/73	0.11/37
SON	0.11/42	0.12/53	0.13/62	0.13/74	0.11/73	0.11/36
			AOD_{CALIOP} (%PBL,%FT)			
DJF	0.11 (64,36)	0.11 (67,33)	0.15 (68,32)	0.09 (61,39)	0.13 (59,41)	0.14 (72,28)
MAM	0.11 (54,46)	0.10 (53,47)	0.12 (58,42)	0.10 (30,70)	0.07 (30,70)	0.12 (58,42)
JJA	0.11 (53,47)	0.11 (44,56)	0.10 (46,54)	0.11 (20,80)	0.08 (11,89)	0.08 (49,51)
SON	0.09 (63,37)	0.10 (57,43)	0.10 (65,35)	0.08 (47,53)	0.07 (35,65)	0.10 (69,31)
			PBLH (m)/RH_{PBL}(%)/RH_{FT}(%)			
DJF	1018/78/37	1156/76/43	1364/79/46	1013/76/52	926/76/58	1198/80/43
MAM	903/77/41	955/72/43	1043/75/48	722/72/53	568/79/55	966/79/50
JJA	775/81/62	725/81/60	697/81/59	481/78/53	351/85/55	713/82/58
SON	1018/80/50	1094/76/45	1181/76/42	825/71/43	593/77/51	1095/81/48

We next compare MERRA-2 speciated aerosol concentrations at the surface (Figure S2) to those of speciated AOD (Figure S1). Surface mass concentrations have the limitation of being biased by larger particles (similar to extinction). The seasonal cycle of mean values for speciated AOD and surface concentration for individual sub-domains generally agree with the exception that there was disagreement for sulfate in each sub-domain (see seasonal mean values in Table S1). Sulfate exhibited higher AODs in JJA but with surface concentrations usually highest in DJF or MAM; although differences in seasonal mean mass concentrations were relatively small (< 1 μg m^{-3}), a plausible explanation is enhanced secondary production of sulfate via oxidation of SO_2 or DMS convectively lifted to the free troposphere in JJA. An important result confirmed by the surface mass concentrations is that sea salt is an order of magnitude higher than the other species, supporting the previous speculation that sea salt dominates the aerosol extinction in the PBL from CALIOP.

459
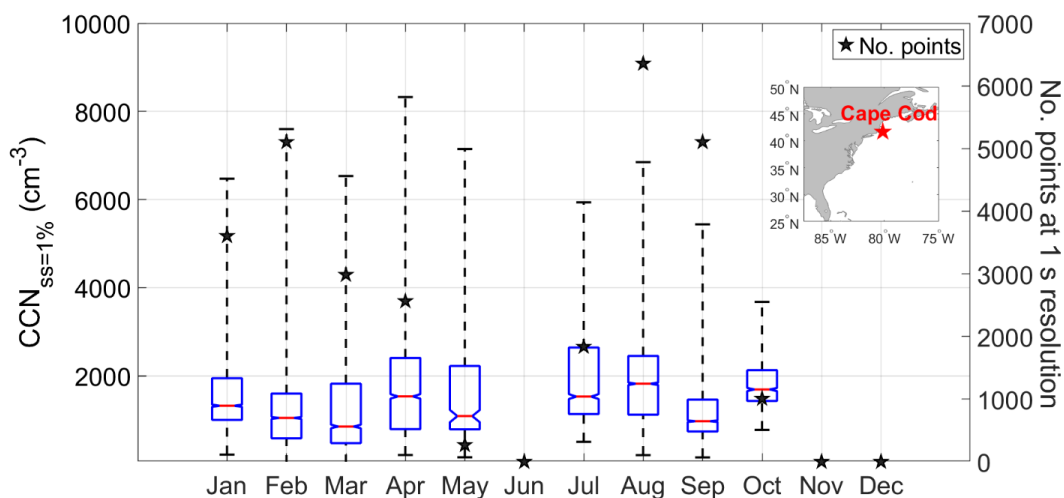
Figure 4: Monthly statistics of CCN concentration (1% supersaturation) measured at Cape Cod between July 2012 and May 2013. Red lines represent median, whiskers are the monthly range, and the top and bottom of boxes represent the 75th and 25th percentile, respectively. The notches in the box plots demonstrate whether medians are different with 95% confidence.

464
3.5 Aerosol-Cloud Interactions
465

Studies of China's east coast have shown that the aerosol indirect effect is especially strong in wintertime, whereby pollution outflow leads to high N_d and suppressed precipitation (Berg et al., 2008; Bennartz et al., 2011). It is hypothesized that a similar effect is taking place off of North America's east coast, which could in part explain enhanced N_d without necessarily a significant jump in aerosol parameter (e.g., AOD, AI) values. Grosvenor et al. (2018) suggested that high cloud fractions in wintertime off these east coasts relative to other seasons are coincident with strong temperature inversions usually associated with cold air outbreaks that serve to concentrate and confine surface layer aerosols. We examine the relative seasonal strength of the aerosol indirect effect via spatial maps of the following metric commonly used in aerosol-cloud interaction (ACI) studies:

$$ACI = d\ln(N_d)/d\ln(\alpha) \qquad (3)$$

where α represents an aerosol proxy parameter that is represented here as AI, AOD, the speciated sulfate AOD (Sulfate$_{AOD}$), and sulfate surface mass concentration (Sulfate$_{sf\text{-}mass}$). The expected range by common convention is 0 – 1, with higher values suggestive of greater enhancement in N_d for the same increase in the aerosol proxy parameter.

Table 4 shows that DJF usually always exhibits the highest ACI values regardless of the aerosol proxy used, consistent with a stronger aerosol indirect effect in DJF over East Asia. The mean ACI values in DJF using AI, AOD, Sulfate$_{AOD}$, and Sulfate$_{sf\text{-}mass}$ ranged from 0.25 to 0.55, 0.28 – 0.59, 0.25 – 0.53, and 0.22 – 0.47, respectively, depending on the sub-domain. Spatial maps of ACI (Figure 5) do not point to significant geographic features. Coefficients of determination (R^2) when computing seasonal ACI values were generally low (≤ 0.30), with spatial maps of R^2 and data point numbers in Figure S3. Poor correlations are suggestive of the non-linear nature aerosol-cloud interactions (e.g., Gryspeerdt et al., 2017) and the influence of other likely factors such as dynamical processes and turbulence, data spatial resolution and dataset size, cloud adiabaticity, wet scavenging effects, and aerosol size distribution (McComiskey et al., 2009). The results of

this section suggest though that aerosol indirect effects could be strongest in DJF, meaning that N_d values increase more for the same increase in aerosol.

Table 4: Estimated values of ACI calculated four ways (dlog(N_d)/dlog(AOD); dlog(N_d)/dlog(AI); dlog(N_d)/dlog(Sulfate$_{AOD}$); dlog(N_d)/dlog(Sulfate$_{sf-mass}$)) for the sub-domains shown in Figure 2. The ACI values were obtained from log-log regression on average daily values of N_d and each of the aerosol proxy variables including only the pixels with CF$_{low-liq.}$ greater than 0.1. Numbers in parentheses, in order, are R^2 and the number of points used for linear regression. Statistically insignificant ACI values with p-value greater than 0.05 are marked by bold font.

	S	C-S	C	C-N	N	Bermuda
			ACI-AI			
DJF	0.55 (0.24,440)	0.53 (0.17,421)	0.53 (0.14,403)	0.33 (0.05,418)	0.25 (0.04,403)	0.42 (0.09,422)
MAM	0.21 (0.03,451)	0.13 (0.01,439)	0.30 (0.06,422)	0.17 (0.02,426)	0.31 (0.05,428)	0.28 (0.04,437)
JJA	0.25 (0.02,437)	0.20 (0.03,437)	0.28 (0.07,424)	0.11 (0.01,430)	-0.12 (0.01,408)	0.38 (0.09,443)
SON	0.23 (0.03,435)	0.20 (0.03,428)	0.26 (0.05,431)	0.19 (0.04,412)	0.24 (0.06,394)	**0.00 (0.00,428)**
all	0.27 (0.05,1763)	0.16 (0.02,1725)	0.22 (0.04,1680)	0.12 (0.01,1686)	0.12 (0.01,1633)	0.23 (0.04,1730)
			ACI-AOD			
DJF	0.59 (0.13,440)	0.53 (0.12,421)	0.47 (0.10,403)	0.39 (0.06,418)	0.28 (0.04,403)	0.37 (0.08,422)
MAM	0.26 (0.02,451)	0.22 (0.01,439)	0.43 (0.07,422)	0.30 (0.04,426)	0.40 (0.06,428)	0.32 (0.03,437)
JJA	**0.02 (0.00,437)**	0.24 (0.02,437)	0.36 (0.07,424)	0.15 (0.01,430)	**-0.06 (0.00,408)**	0.30 (0.04,443)
SON	0.14 (0.01,435)	0.18 (0.02,428)	0.17 (0.02,431)	0.16 (0.02,412)	0.27 (0.05,394)	0.18 (0.02,428)
all	0.13 (0.01,1763)	0.12 (0.01,1725)	0.22 (0.03,1680)	0.15 (0.01,1686)	0.16 (0.02,1633)	0.31 (0.05,1730)
			ACI-Sulfate$_{AOD}$			
DJF	0.53 (0.25,440)	0.53 (0.21,421)	0.53 (0.19,403)	0.37 (0.08,418)	0.25 (0.05,403)	0.43 (0.13,422)
MAM	0.29 (0.05,451)	0.27 (0.04,439)	0.42 (0.14,422)	0.32 (0.07,426)	0.41 (0.11,428)	0.34 (0.07,437)
JJA	0.21 (0.02,437)	0.19 (0.03,437)	0.33 (0.09,424)	0.20 (0.04,430)	**0.04 (0.00,408)**	0.39 (0.09,443)
SON	0.16 (0.02,435)	0.23 (0.04,428)	0.29 (0.07,431)	0.28 (0.09,412)	0.35 (0.13,394)	**0.07 (0.00,428)**
all	0.23 (0.04,1763)	0.19 (0.03,1725)	0.30 (0.07,1680)	0.23 (0.05,1686)	0.22 (0.05,1633)	0.25 (0.05,1730)
			ACI-Sulfate$_{sf-mass}$			
DJF	0.44 (0.29,440)	0.41 (0.22,421)	0.47 (0.22,403)	0.22 (0.04,418)	0.23 (0.06,403)	0.32 (0.14,422)
MAM	0.24 (0.07,451)	0.25 (0.08,439)	0.29 (0.12,422)	0.24 (0.05,426)	0.36 (0.09,428)	0.16 (0.04,437)
JJA	0.11 (0.01,437)	0.12 (0.03,437)	0.23 (0.11,424)	0.19 (0.06,430)	-0.12 (0.01,408)	0.20 (0.07,443)
SON	0.32 (0.16,435)	0.36 (0.18,428)	0.34 (0.19,431)	0.19 (0.06,412)	0.21 (0.05,394)	0.17 (0.07,428)
all	0.32 (0.13,1763)	0.30 (0.12,1725)	0.36 (0.17,1680)	0.19 (0.04,1686)	0.15 (0.02,1633)	0.25 (0.11,1730)

504
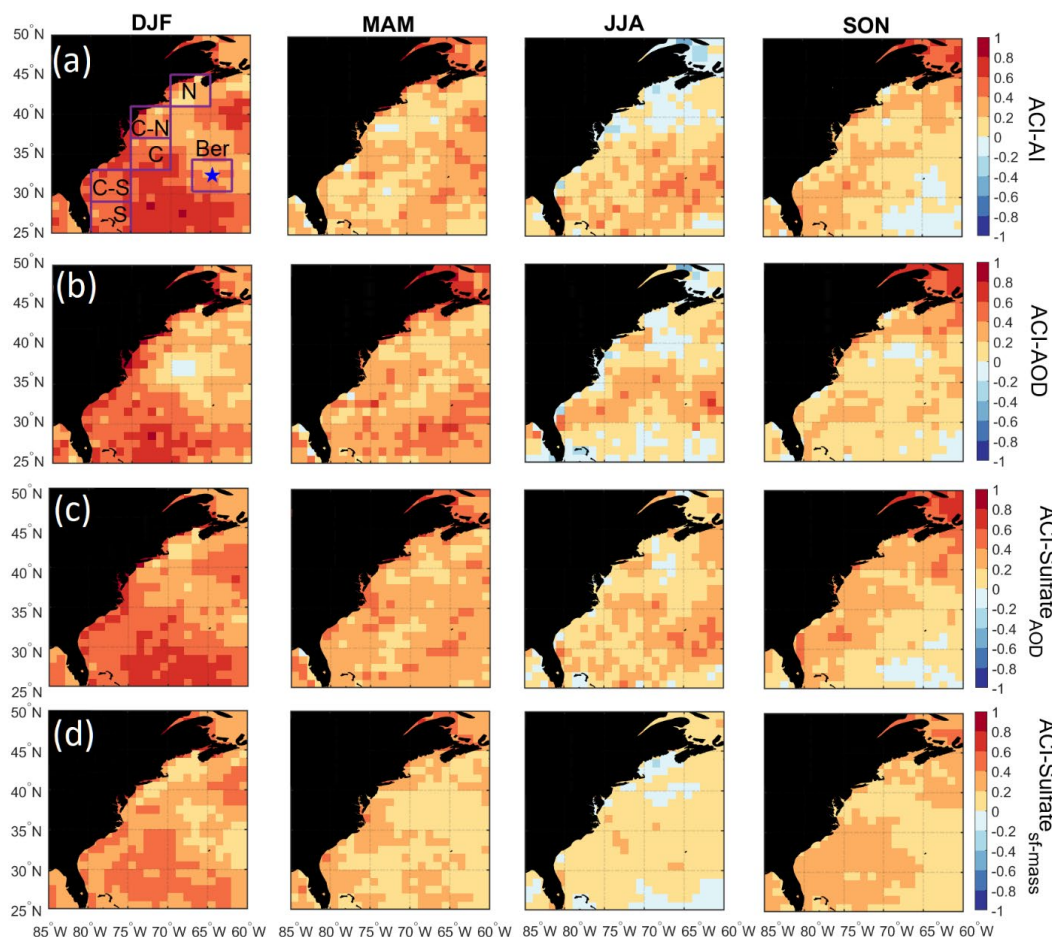
Figure 5: Seasonal maps of the aerosol-cloud interaction (ACI) parameters over the WNAO using daily
N_d and four different aerosol proxy parameters (AI, AOD, Sulfate$_{AOD}$, Sulfate$_{sf-mass}$) from CERES-
MODIS and MERRA-2, respectively. ACI statistics associated with the six sub-domains shown are
summarized in Table 4.

509

4. Discussion of Potential Influential Factors

511   We probe deeper into factors related to the N_d seasonal cycle by using (Section 4.1) composite
512 analyses based on "high" and "low" N_d days, and (Section 4.2) advanced regression techniques tackling non-
513 linear relationships. We focus the analyses on one sub-domain (C-N) both for simplicity and intriguing
514 characteristics: (i) among the highest anthropogenic AOD values over the WNAO, (ii) significant seasonal
515 changes in fractional AOD contribution to the PBL, (iii) close to the Cape Cod site where CCN data were
516 shown, and (iv) the aerosol indirect effect (Table 4) is strongest (weakest) in DJF (JJA).

517

4.1 Composite Analysis

519   Discussion first addresses the behavior of different environmental parameters on days with the highest
520 and lowest N_d values. Seasonal histograms of averaged daily N_d were generated for sub-domain C-N. The
521 histograms are based on the natural logarithm of N_d to better resemble a normal distribution. Subsequently,
522 one standard deviation from both sides of the seasonal mean defined cut-off points outside of which we assign

523   values as being low and high in each season. Cut-off N_d values (cm^{-3}) are as follows (low/high): 33/153
524   (DJF), 29/118 (MAM), 38/100 (JJA), and 31/115 (SON). Next, composite maps for these groups were created
525   (Figures 6 – 10) for sea level pressure, near-surface wind, low-level cloud fraction, cold-air outbreak index,
526   and AOD. The figures contrast the low and high N_d maps with those showing mean seasonal values to
527   investigate potential factors that contribute to seasonal N_d variability. Interested readers are referred to
528   Figures S4 – S21 where similar composite map results are shown for N_d itself and other parameters including
529   those in Table 2.
530
531   The resulting composite maps indicate high N_d days are characterized by (i) reduced SLP; (ii) more northerly-
532   northwesterly flow for all seasons (except JJA) and especially stronger winds in DJF and SON; (iii) higher
533   low-level liquid cloud fraction, especially in DJF; (iv) higher CAO index in the seasons when CAO events
534   occur more frequently (DJF, SON, MAM); and (v) enhanced AOD. Low N_d days generally exhibited opposite
535   conditions when compared to seasonal mean values: (i) enhanced SLP; (ii) wind ranging from southerly to
536   westerly without any significant wind speed enhancement; (iii) reduced low-level liquid cloud fraction,
537   especially in DJF; (iv) lower CAO index in DJF, SON, and MAM; and (v) reduced AOD in DJF and MAM,
538   enhanced AOD in JJA, and limited change in SON. Noteworthy results from Figures S4 – S21 included the
539   enhancement/reduction of PBLH on high/low N_d days (least pronounced in JJA), higher/lower RH at 950 and
540   800 hPa on high/low N_d days, and higher/lower sulfate AOD and surface concentrations on high/low N_d days
541   for DJF and MAM. Furthermore, there was a general reduction in rain on low N_d days for most seasons
542   except SON, with rain enhancement on high N_d days except for DJF (Figure S7); this was unexpected as wet
543   removal was hypothesized to be a reason for reduced N_d for at least the low N_d days. This may be attributed
544   to the rain product being for surface precipitation (and thus not capturing all drizzle) and for all cloud types,
545   including more heavily precipitating clouds deeper and higher than the low-level clouds examined for N_d.

546   The mean seasonal climatological values and anomalies suggest that high N_d cases are marked by
547   continental outflow, high cloud fractions, high PBLH, and low SLP, all of which occur most commonly in
548   DJF and are associated with cold air outbreaks. These events are marked by cold air over the warm ocean
549   leading to strong surface heat fluxes, boundary layer deepening, weakened inversion strength, in addition to
550   high and deep clouds (Kolstad et al., 2009; Fletcher et al., 2016; Abel et al., 2017; Brummer, 1996; Naud et
551   al., 2018). Coincident with these features is the Icelandic Low, which is a significant climatological feature
552   of the North Atlantic whereby subpolar low pressure builds in extratropic areas beginning in the fall with
553   westerly winds in the boundary layer that shift more to northerly in the winter (Sorooshian et al.,
554   2020;Painemal et al., 2021). This low-pressure system seems to be stronger on high N_d days resulting in more
555   continental outflow and high number concentrations of CCN; the greater CAO index values near the coast
556   promote high cloud coverage affording more opportunity for cloud processing of particles to ultimately
557   enhance droplet activation. While there can be considerable enhancement in N_d as cold air outbreak air masses
558   evolve over warmer waters, precipitation scavenging farther downwind will be an efficient method of
559   boundary layer aerosol (and N_d) removal (Abel et al., 2017; Lloyd et al., 2018), which contributes at least in
560   part to the sharp N_d gradients offshore demonstrated in Figure 1.
561
562
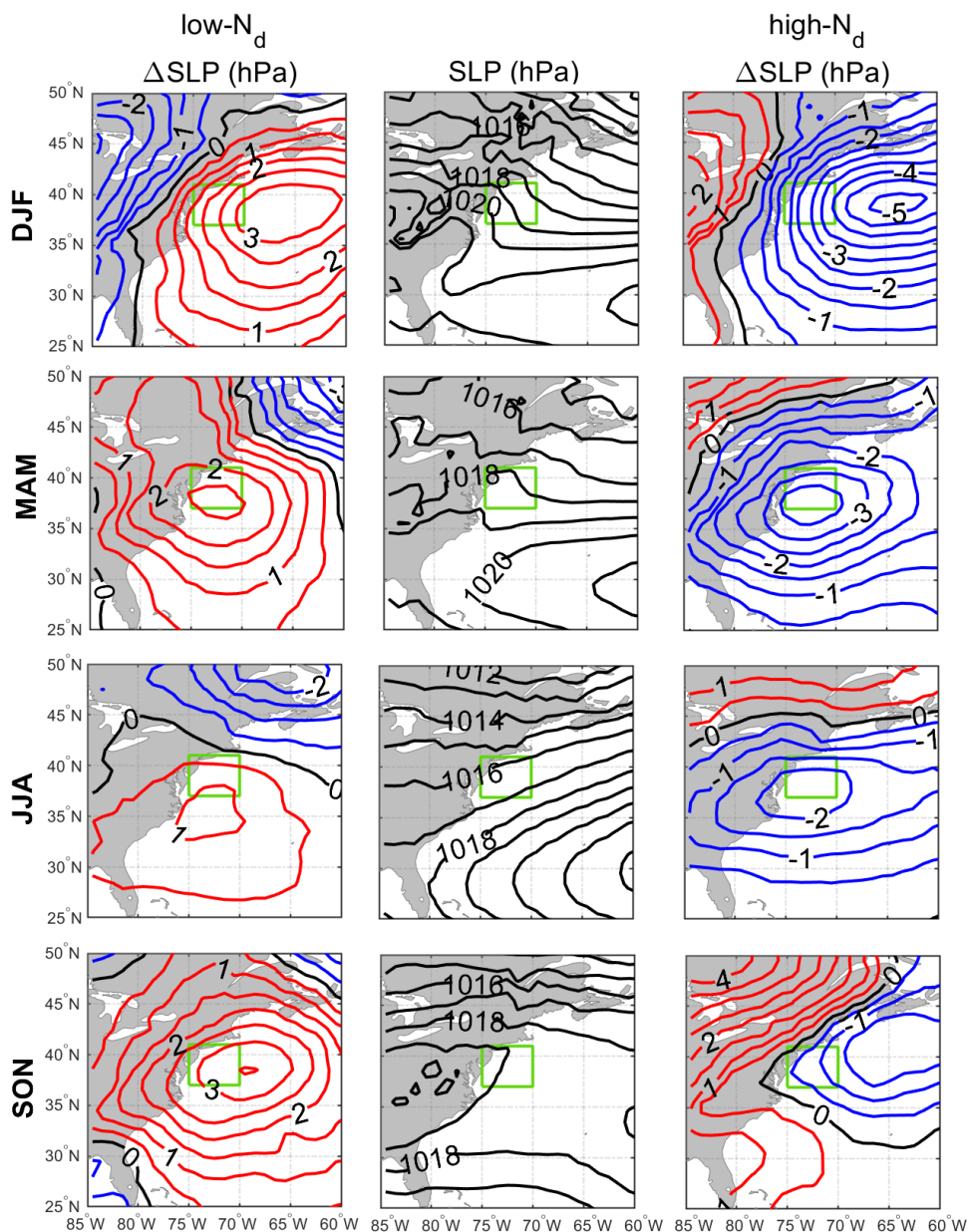
Figure 6: Seasonal climatology of sea-level pressure (SLP) (middle column) and anomalies from seasonal averages for low-N_d days (left column) and high-N_d days (right column). In the left and right columns, red and blue contours are associated with positive and negative anomalies from the climatology, respectively. The green box represents sub-domain C-N for which the analysis was conducted.
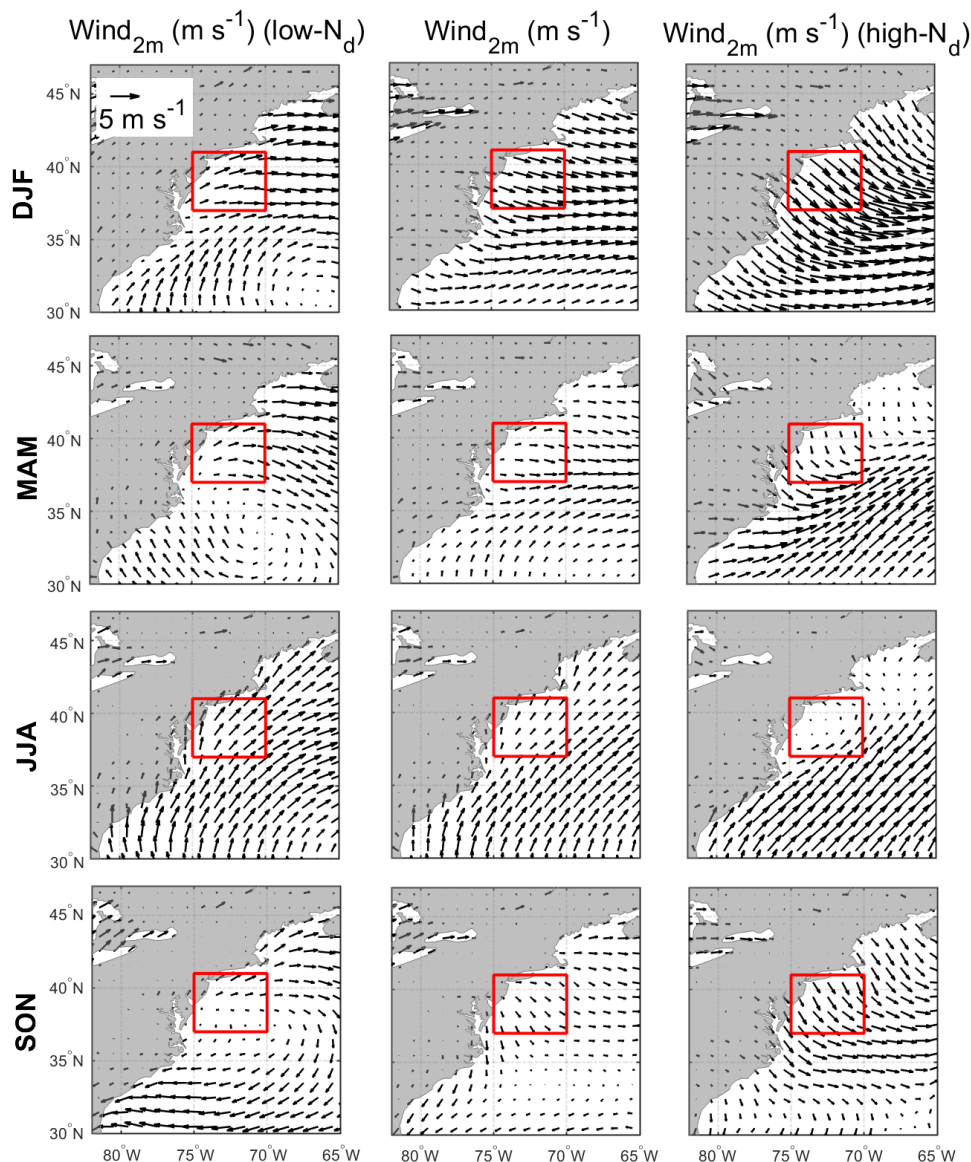
Figure 7: Seasonal climatology of near-surface (2 m above ground) wind speed (middle column) and mean values for low-N_d days (left column) and high-N_d days (right column). The reference wind vector is shown on the top left panel. The red box represents sub-domain C-N for which the analysis was conducted.

569

570
571
572
573
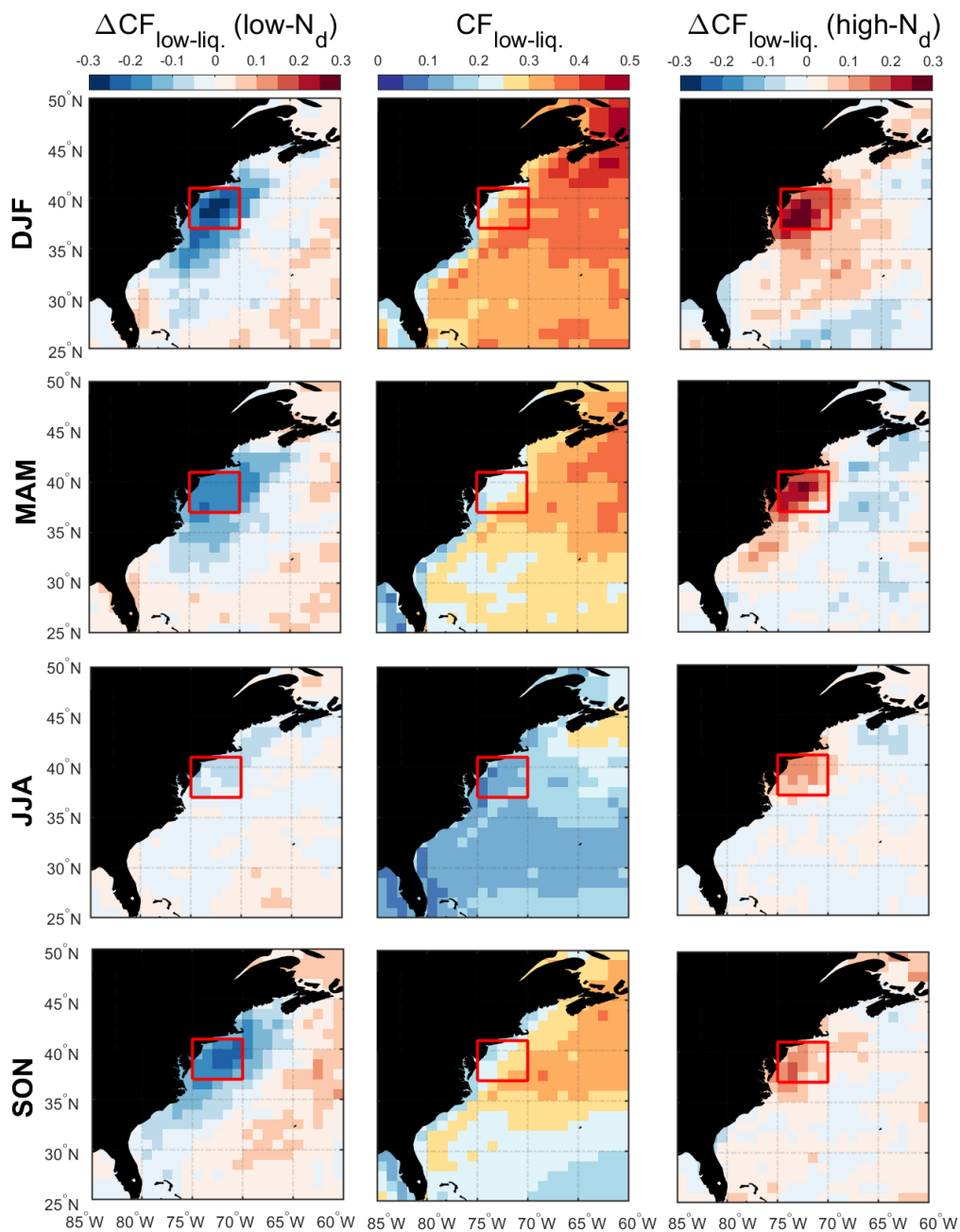
574
Figure 8: Seasonal averages of low-level liquid cloud fraction (middle column) and associated
anomalies on low-N_d days (left column) and high-N_d days (right column). The red box represents sub-
domain C-N for which the analysis was conducted.
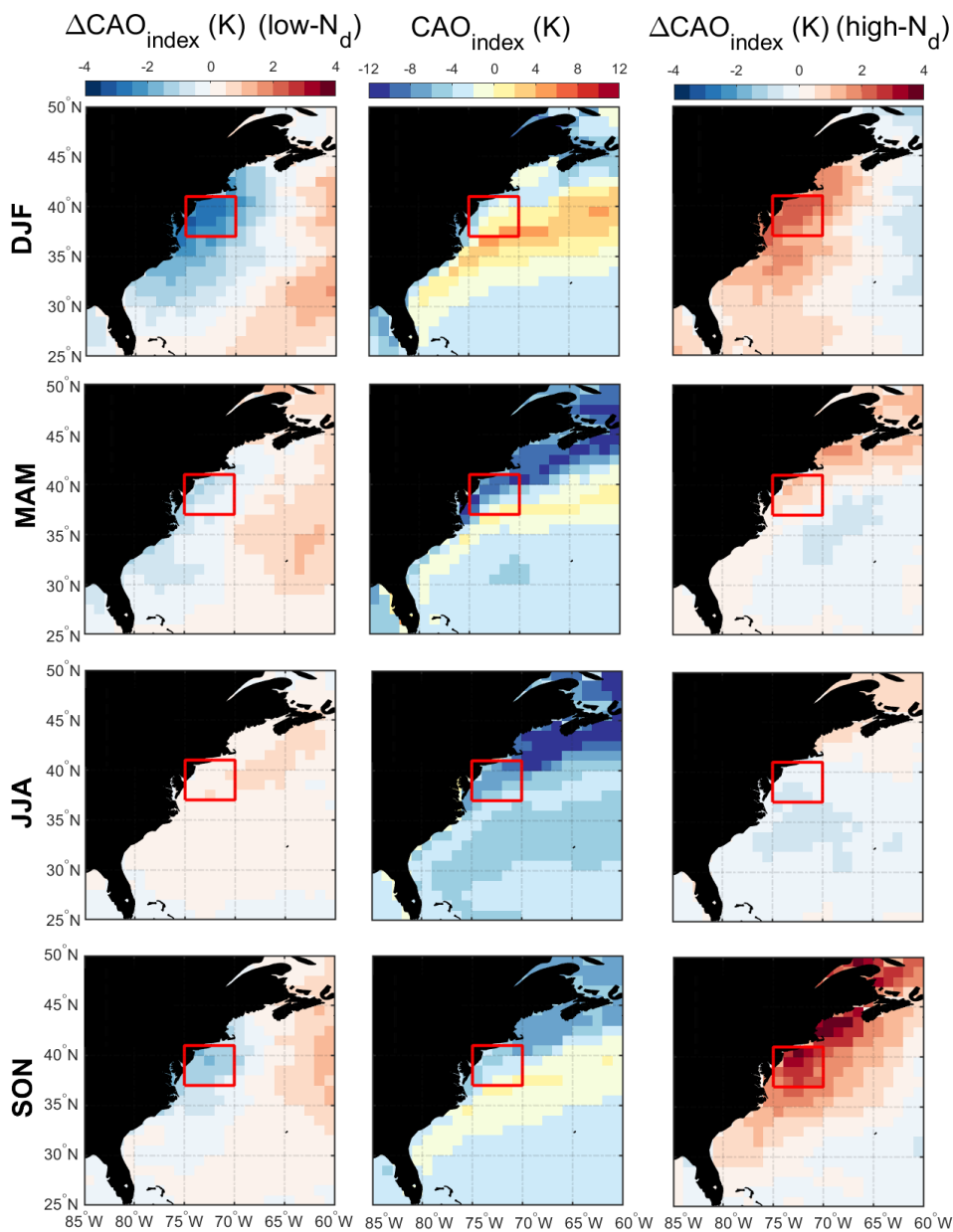
578
579 **Figure 9: Seasonal averages of cold-air outbreak (CAO) index (middle column) and associated**
580 **anomalies on low-N_d days (left column) and high-N_d days (right column). The red box represents sub-**
581 **domain C-N for which the analysis was conducted.**
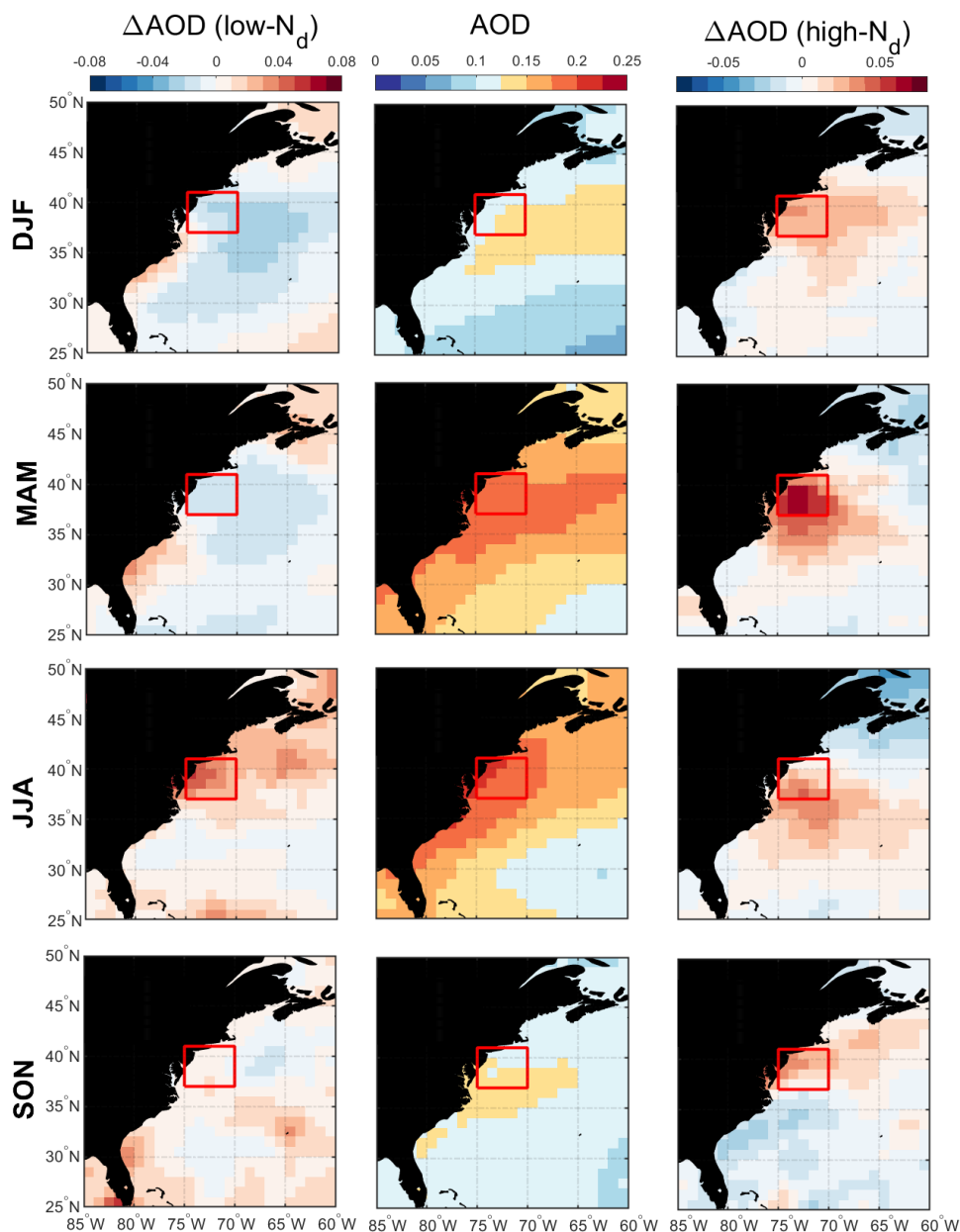
Figure 10: Seasonal averages of MERRA-2 AOD (middle column) and associated anomalies on low-N_d days (left column) and high-N_d days (right column). The red box represents sub-domain C-N for which the analysis was conducted.

4.2 Multivariate Regression Analysis

Modeling analysis focuses on the two seasons (DJF and JJA) with the extremes in terms of seasonal mean values for N_d and aerosol parameters. Added motivation for examining those two seasons stems from spatial maps of R^2 based on ACI analysis (Figure S3). Using the surface sulfate concentration as the aerosol proxy generally yielded higher R^2 values in three seasons (DJF = 0.13, MAM = 0.05, SON = 0.08) except JJA (0.02) for which the choice did not matter owing to low R^2 (≤ 0.03) values for all four aerosol proxy variables tested. Although the R^2 values are all generally low, DJF and JJA are the seasons when surface sulfate levels are the most and least capable in explaining N_d, with R^2 among the four proxy variables exhibiting the widest (DJF values: $0.07 - 0.13$) and narrowest range (JJA: $0.01 - 0.03$) of values. We address here how much improvement is gained in modeling N_d by advancing from linear regressions based on one input variable to (i) adding more input variables, and (ii) moving to a more sophisticated model (GBRT) that captures non-linear relationships.

We show in Table 5 the performance of two linear models based on a single linear regression (with sulfate mass concentration), and a multi-regression that uses 12 input variables listed in Table 2. In addition, Table 5 also lists the performance of the GBRT model that ingests 12 inputs variables, similar to the linear multi-regression model. The average R^2 scores of the test set for predicting N_d based on a linear regression using only sulfate surface mass concentration were 0.17 and 0.09 in DJF and JJA, respectively. In contrast, R^2 between the multi-regression linear model and the test dataset increased to 0.28 and 0.26 for DJF and JJA, respectively. This increase in predictive capability was helpful to reduce the gap between seasons by presumably accounting for factors more important in JJA aside from surface concentration of sulfate. The R^2 scores increased even more to 0.45 and 0.39 for DJF and JJA, respectively, for the GBRT model. Therefore, accounting for non-linear relationships improved predictive capability in both seasons. It is important to note that the GBRT model was robust in terms of overfitting and especially generalizability as R^2 values of the test and validation sets were similar for both seasons.

Table 5: Performance of different models in predicting N_d assessed based on average R^2-scores on both validation and test sets. The models were fitted separately for DJF and JJA seasons. Table 2 has the complete list of variables used in the GBRT model.

Model	Model type	Number of predictor variables	R^2-score (DJF/JJA)	
			Validation set	Test set
$N_d \sim f(Sulfate_{sf-mass})$	Linear	1	0.17/0.10	0.17/0.09
$N_d \sim f(Sulfate_{sf-mass}, CF_{low-liq}, ...)$	Linear	12	0.28/0.27	0.28/0.26
$N_d \sim f(Sulfate_{sf-mass}, CF_{low-liq}, ...)$	GBRT	12	0.45/0.42	0.45/0.39

We next discuss the importance ranking of different parameters from Table 2 in terms of influencing N_d for DJF and JJA (Figure 11). Low-level liquid cloud fraction was the most important parameter in both seasons with the next three parameters being in common but in different order per season. In DJF, sulfate surface mass concentrations were the second most important factor, followed by organic carbon surface concentrations and the CAO index. As sulfate is secondarily produced via gas-to-particle conversion processes, this result is consistent with those from Figure 1 showing the presumed strong impact of particles smaller than 100 nm in impacting N_d values close to shore. In JJA, the CAO index was second most important, followed by organic carbon and sulfate surface concentrations. Also, our results throughout the study and supported by modeling are in agreement with Quinn et al. (2017) that sulfate particles contribute more to the CCN budget than sea salt particles. In DJF and JJA, the fifth most important factor was low-level liquid cloud-top effective height (10th most important in JJA) and PBLH (8th most important in DJF), respectively.
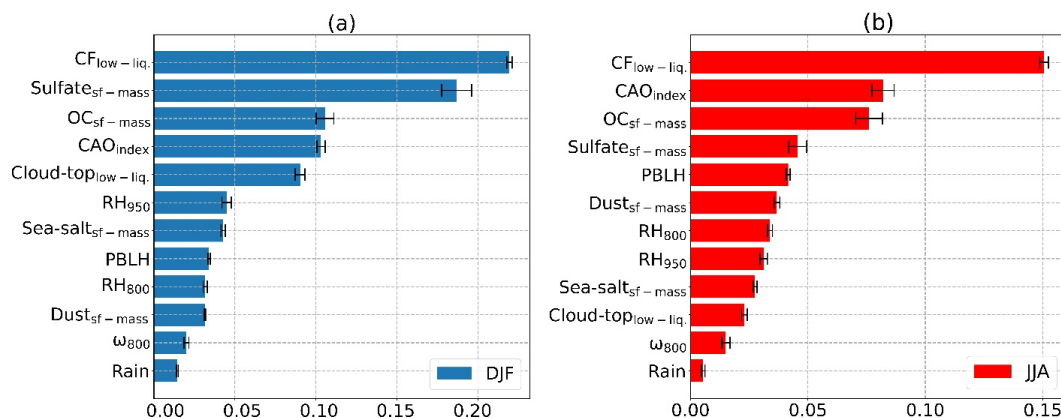
630
631
632 **Figure 11: Average permutation feature importance of input parameters for (a) DJF and (b) JJA based**
633 **on GBRT models trained in each season. Feature importance values were calculated based on using**
634 **the test set. Error bars exhibit the range of feature importance values stemming from the variability**
635 **of the obtained models from the cross-validation resampling procedure**

636
637   Figures 12 and 13 show accumulated local effect (ALE) plots for the various parameters ranked in
638 Figure 11. In both seasons, but especially DJF, enhanced surface concentrations of sulfate and organic carbon
639 coincide with higher N_d, whereas there was not any obvious positive association between N_d and either sea
640 salt or dust (Figure 12). Dust in JJA and sea salt in DJF, seasons of which each respective aerosol type is
641 most predominant, exhibited negative relationships with N_d. Such a negative relationship is plausibly related
642 to differences between ACI when calculated using AOD versus AI (Painemal et al., 2021); for instance,
643 coarse sea salt can expedite collision-coalescence and thus reduce N_d, which has the effect of reducing ACI
644 (Eq. 3) and even possibly yielding negative values (Table 4). Negative values of other ACI constructs
645 coincident with poor R^2 values have previously been attributed to potential effects of giant CCN (Terai et al.,
646 2015; Dadashazar et al., 2017), but further research needs to examine this in more detail.
647   Figure 13 shows the similarity in the positive relationship between cloud fraction and N_d in both
648 seasons. Only in DJF did cloud-top effective height exhibit a clear relationship with N_d (positive), likely
649 linked to the common phenomenon of CAOs noted in Section 4.1 based on heightened CAO index values,
650 deepening of the boundary layer, and weakened inversion strength. This is supported by enhanced N_d values
651 coincident with negative values for ω_{800} (i.e., rising motion) and CAO index values above 0 in DJF without
652 such relationships in JJA (Figure 13). The four parameters in Figure S22 (PBLH, RH_{950}, RH_{800}, Rain) did
653 not reveal very pronounced trends with N_d in either season consistent with how they did not rank highly in
654 importance (Figure 11).
655
656

657
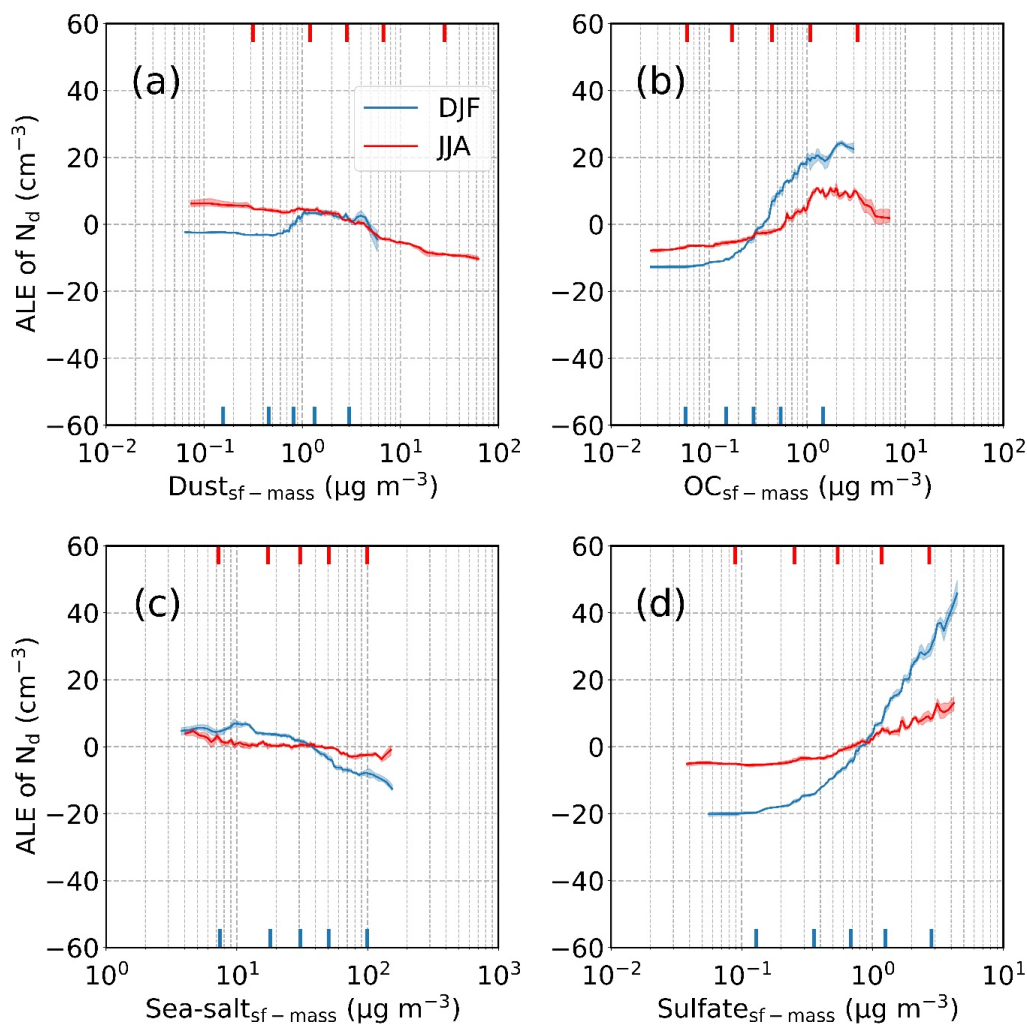
Figure 12: Average local accumulated effect (ALE) profiles based on GBRT modeling for surface mass concentrations of the following parameters: (a) dust, (b) organic carbon, (c) sea-salt, and (d) sulfate. Blue and red profiles represent ALEs of DJF and JJA, respectively. Shaded areas show the ALE ranges stemming from the variability of the obtained models from the cross-validation resampling procedure. Markers on the bottom and top x-axes denote the values of 5th, 25th, 50th, 75th, and 95th percentiles for each input variable.

664
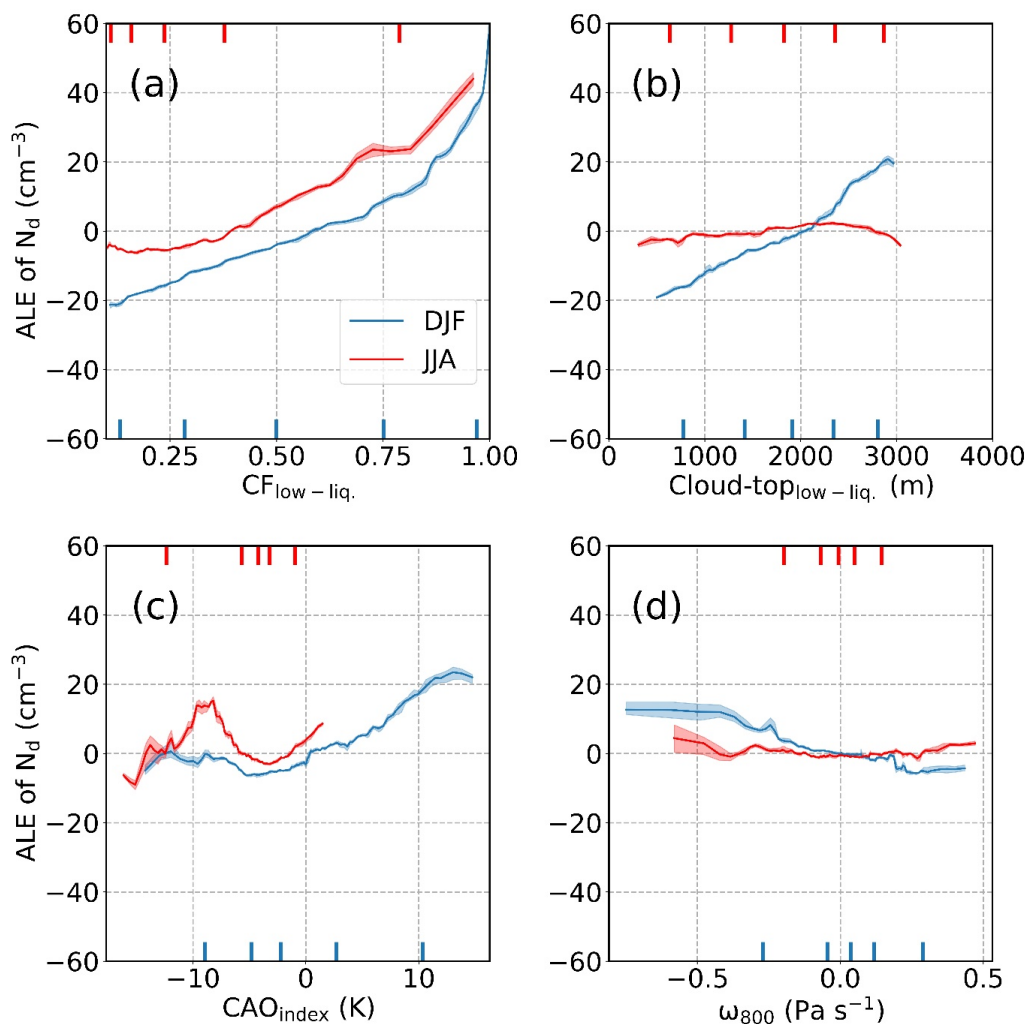
Figure 13: Same as Figure 12 but for the following input parameters: (a) low-level liquid cloud fraction (CF$_{low-liq.}$), (b) cloud-top effective height of low-level liquid cloud (cloud-top$_{low-liq.}$), (c) cold-air outbreak (CAO) index, and (d) vertical pressure velocity at 800 hPa (ω$_{800}$).

4.3 Unexplored Factors

Additional factors impacting the relationship between aerosol and N_d seasonal cycles are discussed here that warrant additional research with more detailed data at finer scales such as with aircraft. We are cognizant that this list is not fully exhaustive. As low-level cloud fraction impacted model results of Section 4.2 so substantially, the dynamics of the studied clouds require further characterization. As cloud fraction and CAO index are well related, especially in DJF, aerosol-cloud interactions likely are stronger than other seasons (as implied by Section 3.5) due in part to enhanced surface fluxes and turbulence, and thus more droplet activation with higher cloud supersaturations (Painemal et al., 2021); in contrast, the smaller shallow cumulus clouds in summertime may be less favorable for droplet activation due to factors such as reduced turbulence and more lateral entrainment.

680   Entrainment of free tropospheric aerosol can impact N_d values, with potentially varying degrees of
681   influence between seasons. It is presumed that with summertime convection, the more broken cumulus scenes
682   are less adiabatic through the cloudy column and more affected by entrainment and mixing; hence, N_d values
683   derived using data that remote sensors retrieve near cloud top could be considerably lower than values lower
684   by cloud base. Satellite remote sensing studies of aerosol-cloud interactions will struggle for analyzing winter
685   data as compared to summertime because of the varying degree of spatial and temporal mismatch in different
686   seasons between cloud and aerosol retrievals. More specifically, it is easier to get nearly coincidental
687   sampling in summertime due to lower cloud fractions, while in winter the frontal regions with high cloud
688   fractions make it challenging to get aerosol retrievals. There is complexity in understanding how aerosols
689   relate to N_d due to how giant CCN can reduce N_d and also since wet scavenging can remove aerosols
690   efficiently. As aircraft data are limited and difficult to use for assessing seasonal cycles, new techniques of
691   retrieving CCN and N_d from space will greatly assist such types of studies in the future.
692
693   **5. Conclusions**

694   This work investigates the seasonal cycle of N_d over the WNAO region in terms of concentration
695   statistics and with discussion of potential influential factors. The results of this work have implications for
696   increased understanding of aerosol-cloud interactions and meteorological factors influencing concentration
697   of cloud droplets in the marine boundary layer. The results and interpretations can be summarized as follows
698   in the order of how they were presented:
699

700   • An ACTIVATE case flight during the DJF season shows a sharp offshore N_d gradient ranging from
701   > 1000 cm^{-3} to < 50 cm^{-3} explained in part by particles smaller than 100 nm activating into drops
702   during a cold air outbreak with post-frontal clouds. There were significant changes in aerosol
703   composition in cloud-free air and also in droplet residual particles as a function of offshore distance.

704   • N_d is generally highest (lowest) in DJF (JJA) over the WNAO but aerosol parameters such as AOD,
705   AI, and surface-based aerosol mass concentrations and CCN concentrations (1% supersaturation) are
706   generally highest in JJA and MAM and are at (or near) their lowest values in DJF. While aerosol
707   extinction in the PBL is highest in DJF, it is driven largely by sea salt (large but few in number), and
708   thus cannot explain the N_d peak in wintertime.

709   • While relative humidity was generally highest in JJA across the WNAO, the differences between
710   seasons in the PBL and FT were not sufficiently large to explain the divergent seasonal cycles of
711   AOD and N_d.

712   • The susceptibility of N_d to aerosols (Eq. 3) was strongest in DJF using four different proxy variables
713   for aerosols, suggestive of at least one reason why N_d can be highest when aerosol proxy variables
714   for concentration are typically near or at their lowest values.

715   • Composite maps of high versus low N_d days across the WNAO reveal that conditions associated with
716   the highest N_d days, regardless of season (but especially DJF) are reduced sea level pressure, stronger
717   winds aligned with continental outflow, high low-level liquid cloud fraction, higher CAO index and
718   PBLH, and enhanced AOD. Cold air outbreaks are coincident with all of these conditions, especially
719   in the colder months of DJF in sharp contrast to JJA when N_d is lowest.

720   • Gradient boosted regression analysis shows that the most important predictors of N_d in DJF and JJA
721   vary to some extent, but with cloud fraction being the most important parameter, followed by either
722   (for DJF) surface mass concentrations of sulfate and organic carbon and CAO index or (for JJA) CAO
723   index, surface mass concentrations of organic carbon, and sulfate concentrations. Accumulated local
724   effect plots confirm that sulfate and organics help drive the high N_d values via continental outflow,
725   which is assisted in large part by CAO type of conditions such as high cloud fraction and high CAO
726   index.

727   Therefore, the combination of continental pollution outflow and turbulence changes contributed by
728   surface fluxes (manifested in strongest CAO index values in DJF and weakest in JJA) markedly influence
729   the N_d cycle, leading to differing annual cycles in cloud microphysics and aerosols. More detailed data such
730   as from aircraft and modeling can help extend this line of research to confirm these findings and speculations
731   such as how (i) the aerosol indirect effect is strongest in DJF due to boundary layer dynamics such as with
732   more turbulence and mixing than other seasons (Painemal et al., 2021); (ii) enhanced giant CCN in forms
733   such as sea salt and dust can reduce N_d via expediting the collision-coalescence process; and (iii) substantial
734   aerosol removal can occur far offshore as postfrontal clouds associated with CAOs build and then begin to
735   precipitate. The latter hypothesis may help explain why Bermuda (> 1000 km offshore the U.S. East Coast)
736   was the only selected sub-domain in this study to not have a seasonal N_d peak in DJF.
737
738

Data Availability.

CERES-MODIS: https://ceres.larc.nasa.gov/data/

CALIPSO: https://subset.larc.nasa.gov/calipso

PERSIANN-CDR: https://chrsdata.eng.uci.edu/

MERRA-2: https://disc.gsfc. nasa.gov/

TCAP CCN: https://adc.arm.gov/discovery

ACTIVATE Airborne Data: https://www-air.larc.nasa.gov/cgi-bin/ArcView/activate.2019

Author contributions. HD, DP, and MA conducted the analysis. AS and HD prepared the manuscript. All authors contributed by providing input and/or participating in airborne data collection.

Competing interests. The authors declare that they have no conflict of interest.

Acknowledgments. The work was funded by NASA grant 80NSSC19K0442 in support of ACTIVATE, a NASA Earth Venture Suborbital-3 (EVS-3) investigation funded by NASA's Earth Science Division and managed through the Earth System Science Pathfinder Program Office. The authors acknowledge the NOAA Air Resources Laboratory (ARL) for the provision of the HYSPLIT transport and dispersion model and READY website (http://ready.arl.noaa.gov) used in this work.

References

Abel, S. J., Boutle, I. A., Waite, K., Fox, S., Brown, P. R. A., Cotton, R., Lloyd, G., Choularton, T. W., and Bower, K. N.: The Role of Precipitation in Controlling the Transition from Stratocumulus to Cumulus Clouds in a Northern Hemisphere Cold-Air Outbreak, J Atmos Sci, 74, 2293-2314, 10.1175/Jas-D-16-0362.1, 2017.

Ackerman, A.S., Kirkpatrick, M.P., Stevens, D.E., Toon, O.B.: The impact of humidity above stratiform clouds on indirect aerosol climate forcing, Nature 432, 1014–1017, doi:10.1038/nature03174, 2004.

Albrecht, B. A.: Aerosols, Cloud Microphysics, and Fractional Cloudiness, Science, 245, 1227-1230, 10.1126/science.245.4923.1227, 1989.

Aldhaif, A. M, Lopez, D. H., Dadashazar, H., Painemal, D., Peters, A. J., Sorooshian, A.: An Aerosol Climatology and Implications for Clouds at a Remote Marine Site: Case Study over Bermuda, J Geophys Res-Atmos, accepted, 2021.

Apley, D. W., and Zhu, J. Y.: Visualizing the effects of predictor variables in black box supervised learning models, J R Stat Soc B, 82, 1059-1086, 10.1111/rssb.12377, 2020.

Ashouri, H., Hsu, K.-L., Sorooshian, S., Braithwaite, D. K., Knapp, K. R., Cecil, L. D., Nelson, B. R. and Prat, O. P.: PERSIANN-CDR: Daily Precipitation Climate Data Record from Multisatellite Observations for Hydrological and Climate Studies, Bull. Am. Meteorol. Soc., 96(1), 69–83, https://doi.org/10.1175/BAMS-D-13-00068.1, 2015.

Bennartz, R., Fan, J. W., Rausch, J., Leung, L. R., and Heidinger, A. K.: Pollution from China increases cloud droplet number, suppresses rain over the East China Sea, Geophys Res Lett, 38, 10.1029/2011gl047235, 2011.

Berg, L. K., Fast, J. D., Barnard, J. C., Burton, S. P., Cairns, B., Chand, D., Comstock, J. M., Dunagan, S., Ferrare, R. A., Flynn, C. J., Hair, J. W., Hostetler, C. A., Hubbe, J., Jefferson, A., Johnson, R., Kassianov, E. I., Kluzek, C. D., Kollias, P., Lamer, K., Lantz, K., Mei, F., Miller, M. A., Michalsky, J., Ortega, I., Pekour, M., Rogers, R. R., Russell, P. B., Redemann, J., Sedlacek, A. J., Segal-Rosenheimer, M., Schmid, B., Shilling, J. E., Shinozuka, Y., Springston, S. R., Tomlinson, J. M., Tyrrell, M., Wilson, J. M., Volkamer, R., Zelenyuk, A., and Berkowitz, C. M.: The Two-Column Aerosol Project: Phase IOverview

and impact of elevated aerosol layers on aerosol optical depth, J Geophys Res-Atmos, 121, 336-361, 10.1002/2015jd023848, 2016.

Berg, W., L'Ecuyer, T., and van den Heever, S.: Evidence for the impact of aerosols on the onset and microphysical properties of rainfall from a combination of satellite observations and cloud-resolving model simulations, J Geophys Res-Atmos, 113, 10.1029/2007jd009649, 2008.

Boucher, O., and Lohmann, U.: The Sulfate-Ccn-Cloud Albedo Effect - a Sensitivity Study with 2 General-Circulation Models, Tellus B, 47, 281-300, 10.1034/j.1600-0889.47.issue3.1.x, 1995.

Boucher, O., Randall, D., Artaxo, P., Bretherton, C., Feingold, G., Forster, P., Kerminen, V.-M., Kondo, Y., Liao, H., Lohmann, U., Rasch, P., Satheesh, S. K., Sherwood, S., Stevens, B., and Zhang, X. Y.: Clouds and aerosols, in: Climate Change 2013: The Physical Science Basis. Contribution of Working Group I to the Fifth Assessment Report of the Intergovernmental Panel on Climate Change, edited by: Stocker, T. F., Qin, D., Plattner, G.-K., Tignor, M., Allen, S. K., Doschung, J., Nauels, A., Xia, Y., Bex, V., and Midgley, P. M., Cambridge University Press, Cambridge, UK, 571-657, 2013.

Breon, F. M., Tanre, D., and Generoso, S.: Aerosol effect on cloud droplet size monitored from satellite, Science, 295, 834-838, 10.1126/science.1066434, 2002.

Brummer, B.: Boundary-layer modification in wintertime cold-air outbreaks from the arctic sea ice, Bound-Lay Meteorol, 80, 109-125, 10.1007/Bf00119014, 1996.

Buchard, V., Randles, C. A., da Silva, A. M., Darmenov, A., Colarco, P. R., Govindaraju, R., Ferrare, R., Hair, J., Beyersdorf, A. J., Ziemba, L. D., and Yu, H.: The MERRA-2 Aerosol Reanalysis, 1980 Onward. Part II: Evaluation and Case Studies, J Climate, 30, 6851-6872, 10.1175/Jcli-D-16-0613.1, 2017.

Chin, M., Ginoux, P., Kinne, S., Torres, O., Holben, B. N., Duncan, B. N., Martin, R. V., Logan, J. A., Higurashi, A., and Nakajima, T.: Tropospheric Aerosol Optical Thickness from the GOCART Model and Comparisons with Satellite and Sun Photometer Measurements, Journal of the Atmospheric Sciences, 59, 461-483, 10.1175/1520-0469(2002)059<0461:TAOTFT>2.0.CO;2, 2002.

Colarco, P., da Silva, A., Chin, M., and Diehl, T.: Online simulations of global aerosol distributions in the NASA GEOS-4 model and comparisons to satellite and ground-based aerosol optical depth, Journal of Geophysical Research: Atmospheres, 115, https://doi.org/10.1029/2009JD012820, 2010.

Corral, A. F., Braun, R., Cairns, B., Gorooh, V. A., Liu, H., Ma, L., Mardi, A., Painemal, D., Stamnes, S., van Diedenhoven, B., Wang, H., Yang, Y., Zhang, B., and Sorooshian, A.: An Overview of Atmospheric Features Over the Western North Atlantic Ocean and North American East Coast – Part 1: Analysis of Aerosols, Gases, and Wet Deposition Chemistry J Geophys Res-Atmos, 10.1029/2020JD032592, 2021.

Dadashazar, H., Wang, Z., Crosbie, E., Brunke, M., Zeng, X. B., Jonsson, H., Woods, R. K., Flagan, R. C., Seinfeld, J. H., and Sorooshian, A.: Relationships between giant sea salt particles and clouds inferred from aircraft physicochemical data, J Geophys Res-Atmos, 122, 3421-3434, 10.1002/2016jd026019, 2017.

Dadashazar, H., Crosbie, E., Majdi, M. S., Panahi, M., Moghaddam, M. A., Behrangi, A., Brunke, M., Zeng, X. B., Jonsson, H. H., and Sorooshian, A.: Stratocumulus cloud clearings: statistics from satellites, reanalysis models, and airborne measurements, Atmos Chem Phys, 20, 4637-4665, 10.5194/acp-20-4637-2020, 2020.

DeCarlo, P. F., Dunlea, E. J., Kimmel, J. R., Aiken, A. C., Sueper, D., Crounse, J., Wennberg, P. O., Emmons, L., Shinozuka, Y., Clarke, A., Zhou, J., Tomlinson, J., Collins, D. R., Knapp, D., Weinheimer, A. J., Montzka, D. D., Campos, T., and Jimenez, J. L.: Fast airborne aerosol size and chemistry measurements above Mexico City and Central Mexico during the MILAGRO campaign, Atmos Chem Phys, 8, 4027-4048, 10.5194/acp-8-4027-2008, 2008.

Deuze, J. L., Breon, F. M., Devaux, C., Goloub, P., Herman, M., Lafrance, B., Maignan, F., Marchand, A., Nadal, F., Perry, G., and Tanre, D.: Remote sensing of aerosols over land surfaces from POLDER-ADEOS-1 polarized measurements, J Geophys Res-Atmos, 106, 4913-4926, 10.1029/2000jd900364, 2001.

Fletcher, J., Mason, S., and Jakob, C.: The Climatology, Meteorology, and Boundary Layer Structure of Marine Cold Air Outbreaks in Both Hemispheres, J Climate, 29, 1999-2014, 10.1175/Jcli-D-15-0268.1, 2016.

830   Fuchs, J., Cermak, J., and Andersen, H.: Building a cloud in the southeast Atlantic: understanding low-
831   cloud controls based on satellite observations with machine learning, Atmos Chem Phys, 18, 16537-16552,
832   10.5194/acp-18-16537-2018, 2018.
833   Gelaro, R., McCarty, W., Suarez, M. J., Todling, R., Molod, A., Takacs, L., Randles, C. A., Darmenov, A.,
834   Bosilovich, M. G., Reichle, R., Wargan, K., Coy, L., Cullather, R., Draper, C., Akella, S., Buchard, V.,
835   Conaty, A., da Silva, A. M., Gu, W., Kim, G. K., Koster, R., Lucchesi, R., Merkova, D., Nielsen, J. E.,
836   Partyka, G., Pawson, S., Putman, W., Rienecker, M., Schubert, S. D., Sienkiewicz, M., and Zhao, B.: The
837   Modern-Era Retrospective Analysis for Research and Applications, Version 2 (MERRA-2), J Climate, 30,
838   5419-5454, 10.1175/Jcli-D-16-0758.1, 2017.
839   Grandey, B. S., and Stier, P.: A critical look at spatial scale choices in satellite-based aerosol indirect effect
840   studies, Atmos. Chem. Phys., 10, 11459-11470, 10.5194/acp-10-11459-2010, 2010.
841   Grosvenor, D. P., Sourdeval, O., Zuidema, P., Ackerman, A., Alexandrov, M. D., Bennartz, R., Boers, R.,
842   Cairns, B., Chiu, J. C., Christensen, M., Deneke, H., Diamond, M., Feingold, G., Fridlind, A., Hunerbein,
843   A., Knist, C., Kollias, P., Marshak, A., McCoy, D., Merk, D., Painemal, D., Rausch, J., Rosenfeld, D.,
844   Russchenberg, H., Seifert, P., Sinclair, K., Stier, P., van Diedenhoven, B., Wendisch, M., Werner, F.,
845   Wood, R., Zhang, Z. B., and Quaas, J.: Remote Sensing of Droplet Number Concentration in Warm
846   Clouds: A Review of the Current State of Knowledge and Perspectives, Rev Geophys, 56, 409-453,
847   10.1029/2017rg000593, 2018.
848   Gryspeerdt, E., Quaas, J., and Bellouin, N.: Constraining the aerosol influence on cloud fraction, J Geophys
849   Res-Atmos, 121, 3566-3583, 10.1002/2015jd023744, 2016.
850   Gryspeerdt, E., Quaas, J., Ferrachat, S., Gettelman, A., Ghan, S., Lohmann, U., Morrison, H., Neubauer,
851   D., Partridge, D. G., Stier, P., Takemura, T., Wang, H. L., Wang, M. H., and Zhang, K.: Constraining the
852   instantaneous aerosol influence on cloud albedo, P Natl Acad Sci USA, 114, 4899-4904,
853   10.1073/pnas.1617765114, 2017.
854   Hasekamp, O. P., Gryspeerdt, E., and Quaas, J.: Analysis of polarimetric satellite measurements suggests
855   stronger cooling due to aerosol-cloud interactions, Nat Commun, 10, 10.1038/s41467-019-13372-2, 2019.
856   Hastie, T., Tibshirani, R., and Friedman, J.: The elements of statistical learning: data mining, inference and
857   prediction, 2 ed., Springer, 2009.
858   Kim, M. H., Omar, A. H., Vaughan, M. A., Winker, D. M., Trepte, C. R., Hu, Y. X., Liu, Z. Y., and Kim,
859   S. W.: Quantifying the low bias of CALIPSO's column aerosol optical depth due to undetected aerosol
860   layers, J Geophys Res-Atmos, 122, 1098-1113, 10.1002/2016jd025797, 2017.
861   Kolstad, E. W., Bracegirdle, T. J., and Seierstad, I. A.: Marine cold-air outbreaks in the North Atlantic:
862   temporal distribution and associations with large-scale atmospheric circulation, Clim Dynam, 33, 187-197,
863   10.1007/s00382-008-0431-5, 2009.
864   Liu, J. J., and Li, Z. Q.: Aerosol properties and their influences on low warm clouds during the Two-
865   Column Aerosol Project, Atmos Chem Phys, 19, 9515-9529, 10.5194/acp-19-9515-2019, 2019.
866   Lloyd, G., Choularton, T. W., Bower, K. N., Gallagher, M. W., Crosier, J., O'Shea, S., Abel, S. J., Fox, S.,
867   Cotton, R., and Boutle, I. A.: In situ measurements of cloud microphysical and aerosol properties during
868   the break-up of stratocumulus cloud layers in cold air outbreaks over the North Atlantic, Atmos Chem
869   Phys, 18, 17191-17206, 10.5194/acp-18-17191-2018, 2018.
870   Loeb, N. G., Manalo-Smith, N., Su, W. Y., Shankar, M., and Thomas, S.: CERES Top-of-Atmosphere
871   Earth Radiation Budget Climate Data Record: Accounting for in-Orbit Changes in Instrument Calibration,
872   Remote Sens-Basel, 8, 10.3390/rs8030182, 2016.
873   Lowenthal, D. H., Borys, R. D., Choularton, T. W., Bower, K. N., Flynn, M. J., and Gallagher, M. W.:
874   Parameterization of the cloud droplet-sulfate relationship, Atmospheric Environment, 38, 287-292,
875   10.1016/j.atmosenv.2003.09.046, 2004.
876   MacDonald, A. B., Mardi, A. H., Dadashazar, H., Aghdam, M. A., Crosbie, E., Jonsson, H. H., Flagan, R.
877   C., Seinfeld, J. H., and Sorooshian, A.: On the relationship between cloud water composition and cloud
878   droplet number concentration, Atmos Chem Phys, 20, 7645-7665, 10.5194/acp-20-7645-2020, 2020.

McComiskey, A., Feingold, G., Frisch, A. S., Turner, D. D., Miller, M. A., Chiu, J. C., Min, Q. L., and Ogren, J. A.: An assessment of aerosol-cloud interactions in marine stratus clouds based on surface remote sensing, J Geophys Res-Atmos, 114, 10.1029/2008jd011006, 2009.

McCoy, D. T., Bender, F. A. M., Mohrmann, J. K. C., Hartmann, D. L., Wood, R., and Grosvenor, D. P.: The global aerosol-cloud first indirect effect estimated using MODIS, MERRA, and AeroCom, J Geophys Res-Atmos, 122, 1779-1796, 10.1002/2016jd026141, 2017.

McCoy, D. T., Bender, F. A. M., Grosvenor, D. P., Mohrmann, J. K., Hartmann, D. L., Wood, R., and Field, P. R.: Predicting decadal trends in cloud droplet number concentration using reanalysis and satellite data, Atmos Chem Phys, 18, 2035-2047, 10.5194/acp-18-2035-2018, 2018.

Minnis, P., Sun-Mack, S., Young, D. F., Heck, P. W., Garber, D. P., Chen, Y., Spangenberg, D. A., Arduini, R. F., Trepte, Q. Z., Smith, W. L., Ayers, J. K., Gibson, S. C., Miller, W. F., Hong, G., Chakrapani, V., Takano, Y., Liou, K. N., Xie, Y., and Yang, P.: CERES Edition-2 Cloud Property Retrievals Using TRMM VIRS and Terra and Aqua MODIS Data-Part I: Algorithms, Ieee T Geosci Remote, 49, 4374-4400, 10.1109/Tgrs.2011.2144601, 2011.

Minnis, P., Sun-Mack, S., Chen, Y., Chang, F., Yost, C. R., Smith, W. L., Heck, P. W., Arduini, R. F., Bedka, S. T., Yi, Y., Hong, G., Jin, Z., Painemal, D., Palikonda, R., Scarino, B. R., Spangenberg, D. A., Smith, R. A., Trepte, Q. Z., Yang, P., and Xie, Y.: CERES MODIS Cloud Product Retrievals for Edition 4--Part I: Algorithm Changes, Ieee T Geosci Remote, 1-37, 10.1109/TGRS.2020.3008866, 2020.

Molnar, C.: Interpretable Machine Learning. A Guide for Making Black Box Models Explainable, https://christophm.github.io/interpretable-ml-book/, 2019.

Myhre, G., Shindell, D., Bréon, F.-M., Collins, W., Fuglestvedt, J., Huang, J., Koch, D., Lamarque, J.-F., Lee, D., Mendoza, B., Nakajima, T., Robock, A., Stephens, G., Takemura, T., and Zhang, H.: Anthropogenic and natural radiative forcing, in: Climate Change 2013: The Physical Science Basis. Contribution of Working Group I to the Fifth Assessment Report of the Intergovernmental Panel on Climate Change, edited by: Stocker, T. F., Qin, D., Plattner, G.-K., Tignor, M., Allen, S. K., Doschung, J., Nauels, A., Xia, Y., Bex, V., and Midgley, P. M., Cambridge University Press, Cambridge, UK, 659-740, 2013.

Nakajima, T., Higurashi, A., Kawamoto, K., and Penner, J. E.: A possible correlation between satellite-derived cloud and aerosol microphysical parameters, Geophys Res Lett, 28, 1171-1174, 10.1029/2000gl012186, 2001.

Naud, C. M., Booth, J. F., and Lamraoui, F.: Post Cold Frontal Clouds at the ARM Eastern North Atlantic Site: An Examination of the Relationship Between Large-Scale Environment and Low-Level Cloud Properties, J Geophys Res-Atmos, 123, 12117-12132, 10.1029/2018jd029015, 2018.

Nguyen, P., Ombadi, M., Sorooshian, S., Hsu, K., AghaKouchak, A., Braithwaite, D., Ashouri, H. and Thorstensen, A. R.: The PERSIANN family of global satellite precipitation data: a review and evaluation of products, Hydrol. Earth Syst. Sci., 22(11), 5801–5816, https://doi.org/10.5194/hess-22-5801-2018, 2018.

Painemal, D.: Global Estimates of Changes in Shortwave Low-Cloud Albedo and Fluxes Due to Variations in Cloud Droplet Number Concentration Derived From CERES-MODIS Satellite Sensors, Geophys Res Lett, 45, 9288-9296, 10.1029/2018gl078880, 2018.

Painemal, D., Chang, F. L., Ferrare, R., Burton, S., Li, Z., Smith Jr., W. L., Minnis, P., Feng, Y., and Clayton, M.: Reducing uncertainties in satellite estimates of aerosol–cloud interactions over the subtropical ocean by integrating vertically resolved aerosol observations, Atmos Chem Phys, 20, 7167-7177, 10.5194/acp-20-7167-2020, 2020.

Painemal, D., Corral, A. F., Sorooshian, A., Brunke, M. A., Chellappan, S., Gorooh, V. A., Ham, S., O'Neill, L., Smith Jr., W. L., Tselioudis, G., Wang, H., Zeng, X., and Zuidema, P.: An Overview of Atmospheric Features Over the Western North Atlantic Ocean and North American East Coast – Part 2: Circulation, Boundary Layer, and Clouds, J Geophys Res-Atmos, 10.1029/2020JD033423, 2021.

Papritz, L., Pfahl, S., Sodemann, H., and Wernli, H.: A Climatology of Cold Air Outbreaks and Their Impact on Air-Sea Heat Fluxes in the High-Latitude South Pacific, J Climate, 28, 342-364, 10.1175/Jcli-D-14-00482.1, 2015.

Pedregosa, F., Varoquaux, G., Gramfort, A., Michel, V., Thirion, B., Grisel, O., Blondel, M., Prettenhofer, P., Weiss, R., Dubourg, V., Vanderplas, J., Passos, A., Cournapeau, D., Brucher, M., Perrot, M., and Duchesnay, E.: Scikit-learn: Machine Learning in Python, J Mach Learn Res, 12, 2825-2830, 2011.

Penner, J. E., Xu, L., and Wang, M. H.: Satellite methods underestimate indirect climate forcing by aerosols, P Natl Acad Sci USA, 108, 13404-13408, 10.1073/pnas.1018526108, 2011.

Persson, C., Bacher, P., Shiga, T., and Madsen, H.: Multi-site solar power forecasting using gradient boosted regression trees, Sol Energy, 150, 423-436, 10.1016/j.solener.2017.04.066, 2017.

Quaas, J., Boucher, O., and Lohmann, U.: Constraining the total aerosol indirect effect in the LMDZ and ECHAM4 GCMs using MODIS satellite data, Atmos Chem Phys, 6, 947-955, 10.5194/acp-6-947-2006, 2006.

Quaas, J., Boucher, O., Bellouin, N., and Kinne, S.: Satellite-based estimate of the direct and indirect aerosol climate forcing, J Geophys Res-Atmos, 113, 10.1029/2007jd008962, 2008.

Quinn, P. K., Coffman, D. J., Johnson, J. E., Upchurch, L. M., and Bates, T. S.: Small fraction of marine cloud condensation nuclei made up of sea spray aerosol, Nature Geoscience, 10, 674-679, 10.1038/ngeo3003, 2017.

Randles, C. A., da Silva, A. M., Buchard, V., Colarco, P. R., Darmenov, A., Govindaraju, R., Smirnov, A., Holben, B., Ferrare, R., Hair, J., Shinozuka, Y., and Flynn, C. J.: The MERRA-2 Aerosol Reanalysis, 1980 Onward. Part I: System Description and Data Assimilation Evaluation, J Climate, 30, 6823-6850, 10.1175/Jcli-D-16-0609.1, 2017.

Rolph, G., Stein, A. and Stunder, B.: Real-time Environmental Applications and Display sYstem: READY, Environ. Model. Softw., 95, 210–228, https://doi.org/10.1016/j.envsoft.2017.06.025, 2017.

Sekiguchi, M., Nakajima, T., Suzuki, K., Kawamoto, K., Higurashi, A., Rosenfeld, D., Sano, I., and Mukai, S.: A study of the direct and indirect effects of aerosols using global satellite data sets of aerosol and cloud parameters, J Geophys Res-Atmos, 108, 10.1029/2002jd003359, 2003.

Shingler, T., Dey, S., Sorooshian, A., Brechtel, F. J., Wang, Z., Metcalf, A., Coggon, M., Mulmenstadt, J., Russell, L. M., Jonsson, H. H., and Seinfeld, J. H.: Characterisation and airborne deployment of a new counterflow virtual impactor inlet, Atmos Meas Tech, 5, 1259-1269, 10.5194/amt-5-1259-2012, 2012.

Sinclair, K., van Diedenhoven, B., Cairns, B., Alexandrov, M., Moore, R., Ziemba, L. D., and Crosbie, E.: Observations of Aerosol-Cloud Interactions During the North Atlantic Aerosol and Marine Ecosystem Study, Geophysical Research Letters, 47, e2019GL085851, https://doi.org/10.1029/2019GL085851, 2020.

Sorooshian, A., Anderson, B., Bauer, S. E., Braun, R. A., Cairns, B., Crosbie, E., Dadashazar, H., Diskin, G., Ferrare, R., Flagan, R. C., Hair, J., Hostetler, C., Jonsson, H. H., Kleb, M. M., Liu, H. Y., MacDonald, A. B., McComiskey, A., Moore, R., Painemal, D., Russell, L. M., Seinfeld, J. H., Shook, M., Smith, W. L., Thornhill, K., Tselioudis, G., Wang, H. L., Zeng, X. B., Zhang, B., Ziemba, L., and Zuidema, P.: Aerosol-Cloud-Meteorology Interaction Airborne Field Investigations: Using Lessons Learned from the US West Coast in the Design of ACTIVATE off the US East Coast, B Am Meteorol Soc, 100, 1511-1528, 10.1175/Bams-D-18-0100.1, 2019.

Sorooshian, A., Corral, A. F., Braun, R. A., Cairns, B., Crosbie, E., Ferrare, R., Hair, J., Kleb, M. M., Mardi, A. H., Maring, H., McComiskey, A., Moore, R., Painemal, D., Scarino, A. J., Schlosser, J., Shingler, T., Shook, M., Wang, H. L., Zeng, X. B., Ziemba, L., and Zuidema, P.: Atmospheric Research Over the Western North Atlantic Ocean Region and North American East Coast: A Review of Past Work and Challenges Ahead, J Geophys Res-Atmos, 125, 10.1029/2019JD031626, 2020.

Stein, A. F., Draxler, R. R., Rolph, G. D., Stunder, B. J. B., Cohen, M. D. and Ngan, F.: NOAA's HYSPLIT Atmospheric Transport and Dispersion Modeling System, Bull. Am. Meteorol. Soc., 96(12), 2059–2077, https://doi.org/10.1175/BAMS-D-14-00110.1, 2015.

Storelvmo, T., Lohmann, U., and Bennartz, R.: What governs the spread in shortwave forcings in the transient IPCC AR4 models?, Geophys Res Lett, 36, 10.1029/2008gl036069, 2009.

Tackett, J. L., Winker, D. M., Getzewich, B. J., Vaughan, M. A., Young, S. A., and Kar, J.: CALIPSO lidar level 3 aerosol profile product: version 3 algorithm design, Atmos Meas Tech, 11, 4129-4152, 10.5194/amt-11-4129-2018, 2018.

979   Terai, C. R., Wood, R., and Kubar, T. L.: Satellite estimates of precipitation susceptibility in low-level
980   marine stratiform clouds, J Geophys Res-Atmos, 120, 8878-8889, 10.1002/2015jd023319, 2015.
981   Thornhill, K. L., Anderson, B. E., Barrick, J. D. W., Bagwell, D. R., Friesen, R., and Lenschow, D. H.: Air
982   motion intercomparison flights during Transport and Chemical Evolution in the Pacific (TRACE-P)/ACE-
983   ASIA, Journal of Geophysical Research: Atmospheres, 108, https://doi.org/10.1029/2002JD003108, 2003.
984   Twomey, S.: Influence of Pollution on Shortwave Albedo of Clouds, J Atmos Sci, 34, 1149-1152,
985   10.1175/1520-0469(1977)034<1149:Tiopot>2.0.Co;2, 1977.
986   Winker, D. M., Vaughan, M. A., Omar, A., Hu, Y. X., Powell, K. A., Liu, Z. Y., Hunt, W. H., and Young,
987   S. A.: Overview of the CALIPSO Mission and CALIOP Data Processing Algorithms, J Atmos Ocean Tech,
988   26, 2310-2323, 10.1175/2009jtecha1281.1, 2009.
989   Wood, R.: Stratocumulus Clouds, Monthly Weather Review, 140, 2373-2423, 10.1175/Mwr-D-11-00121.1,
990   2012.
991